Universidad
Carlos III de Madrid
www.uc3m.es

TESIS DOCTORAL

Contributions to the quantitative analysis of dynamic PET studies using clustering approaches

Autor
José María Mateos Pérez

Director
Juan José Vaquero López

DEPARTAMENTO DE BIOINGENIERÍA E INGENIERÍA AEROESPACIAL

Leganés, mayo 2014

TESIS DOCTORAL

Contributions to the quantitative analysis of dynamic PET studies using clustering approaches

Autor: José María Mateos Pérez

Director: Juan José Vaquero López

Firma del Tribunal Calificador:

Firma

Presidente:

Vocal:

Secretario:

Calificación:

Leganés, de de

And now for something completely different.
Monty Python.

Table of contents

Abstract

Dynamic positron emission tomography (PET) is a widespread medical imaging technique that allows the quantification of different physiological parameters within the body and yields more information that the one provided by a single, static image. Quantification of these studies involves obtaining the input function, that is, the amount of tracer present in arterial blood at any given point in time, and the tissue time-activity curve (TAC) for the tissue or organ under study. The subjacent biological processes are modelled as the tracer exchange rates between the arterial activity source and a compartmental model; this mathematical approach allows to quantify different biological aspects (metabolic rates, blood flow, specific receptor binding) in a non-invasive way.

Typically, arterial and tissue TACs are extracted from the image data by drawing a ROI over the areas of interest, either over the PET image or over some anatomical imaging modality, such as CT, and in some cases acquire some blood samples to correct the input function for metabolites, partial volume effects or other different sources of distortion that may bias the final result. While this ROI delineation is done normally by an experienced operator, this process is very slow and, more importantly, subjective and non-replicable. Furthermore, ROI delineation over registered anatomical images may group together regions that look identical in the CT image but have different underlying kinetics.

These reasons have motivated the development of automatic segmentation or TAC extraction algorithms, of which there are several examples in the medical imaging literature. Most of the proposed methods involve the use of unsupervised machine learning algorithms or the direct application of dimensionality reduction techniques, such as PCA or SVD. This thesis studies the feasibility of supervised algorithms to extract the activity curves of dynamic studies based solely on the knowledge acquired about the kinetics of similar ones. Our experiments on three swine studies showed that the segmentation was successful and the obtained TACs allowed the computation of the kinetic analysis and obtained smaller errors in the kinetic parameters obtained from the mathematical model than the manual segmentations. Said supervised algorithms are not common in the literature but we have shown that they can be a viable option for very specific subset of cases.

One of the problems of the published automatic segmentation algorithms is the general lack of published source codes or even binary distributions. As has been studied in the literature, this presents a problem by itself, as it forces other researchers to re-implement said algorithms. This work presents the development of an open framework for dynamic imaging clustering that includes the most commonly used algorithms and that can be easily extended by third parties through the use of its public API. The code for said framework has been published with a free software license to allow it to be modified by external researchers and adapt it to their needs. It

has been developed as an ImageJ plugin to take advantage to all the imaging analysis functionalities already presented in said platform.

Using this framework, we also present an improvement of the classical leader-follower algorithm. This unsupervised algorithm groups image voxels with similar TACs according to a threshold set by the user and creates as many clusters as necessary to form homogeneous regions. Due to the nature of the partial volume distortions that need to be removed from the final TACs as much as possible, the proposed method implements a two-step leader-follower modification. In this case, the image voxels are clustered according to both a similarity metric and a distance metric; particularly, the cosine similarity and the Euclidean distance were chosen for our tests. This algorithm successfully segmented all of the evaluated 24 mice imaging studies, yielding quantitative parameters after the kinetic modelling that were not significantly different from those obtained via manual delineation and maintained the differences between the three tracers used in this experiment.

Resumen

La tomografía por emisión de positrones (PET) es una técnica de imagen médica ampliamente utilizada que permite la cuantificación de diferentes parámetros fisiológicos dentro del cuerpo y arroja más información que la que puede obtenerse mediante una única imagen estática. La cuantificación de estos estudios necesita la obtención de la función de entrada, esto es, la cantidad de trazador presente en sangre arterial a lo largo del tiempo, y la curva de actividad (TAC) del tejido u órgano bajo estudio. Los procesos biológicos subyacentes se modelan como las velocidades de intercambio de trazador entre la fuente de actividad arterial y un modelo compartimental; esta aproximación matemática permite cuantificar diferentes aspectos biológicos (metabolismo, flujo sanguíneo, fijación a receptores específicos) de una forma no invasiva.

Típicamente, la función de entrada y la TAC de los tejidos se extraen directamente de la imagen mediante el trazado de una región de interés (ROI), bien sobre la imagen PET directamente o sobre alguna modalidad de imagen que presente información anatómica, como el CT, y en algunos casos requiere la obtención de muestras de sangre para corregir en la función de entrada el efecto de metabolitos, efectos de volumen parcial u otras fuentes de distorsión que pueden sesgar el resultado final. Aunque este proceso de delineación lo realiza habitualmente un operador experimentado, este proceso es lento, subjetivo y no replicable. Además, la delineación de ROIs sobre imágenes anatómicas registradas puede agrupar regiones que aparecen idénticas en la imagen de CT pero tienen diferentes comportamientos cinéticos.

Estas razones han motivado el desarrollo de algoritmos de segmentación automática o extracción de TAC, de los cuáles hay múltiples ejemplos en la literatura de imagen médica. La mayoría de los métodos propuestos son implementaciones de algoritmos de *unsupervised machine learning*, o aprendizaje máquina no supervisado, o la aplicación directa de técnicas de reducción de dimensionalidad, como análisis de componentes principales (PCA) o descomposición en valores singulares (SVD). Esta tesis doctoral estudia la posibilidad de emplear algoritmos supervisados para extraer las curvas de actividad de estudios dinámicos basándose únicamente en el conocimiento adquirido en la cinética de estudios similares. La experimentación con tres estudios porcinos mostró que la obtención de las TACs fue exitosa, y estos datos permitieron el cálculo de los parámetros cinéticos, obteniendo errores en el ajuste matemático menores que los obtenidos mediante una segmentación manual. Este tipo de algoritmos supervisados no son comunes en la literature pero hemos demostrado que pueden ser una opción viable para un subconjunto de casos específico.

Uno de los problemas de los algoritmos de segmentación automática publicados en la literatura es la carencia general de código fuente o incluso distribuciones binarias. Como ya se ha estudiado en la literature, esto presenta un problema, al forzar a investigadores de otras instituciones a reimplementar dichos algoritmos. Este trabajo presenta un marco de desarrollo

para algoritmos de *clustering* aplicados a imagen médica dinámica que incluye los algoritmos más comúnmente utilizados y que puede ser extendido fácilmente mediante terceros a través del uso de su interfaz de programación (API) pública. El código para dicho marco de desarrollo ha sido publicado con una licencia libre para permitir su modificación por investigadores externos y su adaptación a sus necesidades. Se ha programado como un *plugin* de la plataforma de análisis de imagen ImageJ para aprovechar todas las ventajas y funcionalidades de análisis ya presentes en dicha plataforma.

Empleando este marco de desarrollo, finalmente presentamos una mejora sobre un algoritmo clásico *leader-follower*. Este algoritmo no supervisado agrupa vóxeles de la imagen con TACs similares de acuerdo a un umbral establecido por el usuario, y crea tantos *clusters*, o grupos, necesaarios para formar regiones homogéneas. Debido a los efectos de volumen parcial, que deben ser eliminados de las TACs finales lo máximo posible, el método propuesto implementa una modificación del *leader-follower* en dos pasos. En este caso, los vóxeles de la imagen se agrupan de acuerdo a una métrica de similitud (coseno) y una métrica de distancia (Euclídea). El algoritmo segmentó con éxito 24 imágenes dinámicas de ratón, ofreciendo parámetros cuantitativos tras el modelado cinético que no fueron diferentes de forma significativa de los obtenidos a través de la delineación manual y manteniendo las diferencias observadas entre los tres trazadores empleados en este experimento.

1 Introduction

1.1 PET imaging technique

Medical imaging techniques are currently one of the most useful tools for diagnosis in medicine. Noninvasive technologies such as magnetic resonance imaging (MRI), computerized tomography (CT), positron emission tomography (PET) or single photon emission tomography (SPECT) allow observing *in vivo* anatomy, which yields very useful information that was completely unthinkable mere years before.

Particularly, clinical PET use has experimented a considerable increment in the last years, with important applications in oncology, cardiology and neurology, to cite a few medical fields (Bailey et al. 2003; Beller & Bergmann 2004).

This imaging technique uses a radioactive substance in order to acquire maps of radiation distribution within the tissue of interest. Typically, said radioactive substance is chemically bound to a biologically active substance that is injected in amounts small enough to be measured but not as big as to cause biological effects (trace amounts); hence the most commonly used term, *radiotracer*. The biologically active part will define the behavior of the tracer and therefore the type of measurement that will be done with the PET scanner (for instance, metabolism or blood flow measurements).

An uptake period follows the injection in order to let the tracer accumulate in the tissues. Then, the subject is placed inside a ring of detectors (the PET scanner) designed to pinpoint the location of the radioactive substances within the body and generate a dataset that will allow, by means of a mathematical tomographic image reconstruction algorithm, to build a 3D image of the tracer concentration. The acquisition of all the necessary data takes several minutes, depending on the type of study, during which the patient should move as little as possible; in animal studies it is common to sedate the specimen to avoid blurring due to movement in the reconstructed image.

It is also possible to have the image acquisition process starting at the same time as the tracer injection. In this case, several sequential images are acquired in a way that allows the study of the tracer distribution with time. This modality produces the so called dynamic PET studies and this PhD thesis will be focused on them. While a static PET scan provides this useful spatial information (has the glucose being consumed in this tissue an indicator of tumoral activity?), the combination of several sequential acquisitions showing the change in the tracer distribution with time yields additional temporal information that allows to answer more subtle questions such as the absorption rate for a given tissue (Morris et al. 2004).

The physical mechanism that enables the PET image acquisition is the radioactive decay of positron-emitting nuclides. When these particles decay, they emit a positron: the antimatter equivalent of an electron. The rate at which the nuclides disintegrate, emitting positrons, depends on a parameter called the *half-life*, which specifies the time it takes for half the nuclei to decay. As the positron passes through the neighboring matter it will lose energy due to collisions or scatter phenomena, until it reaches a rest state, interacts with an electron from the nearby matter, and produces the gamma rays as a result of the disintegration of the positron-electron pair.

Nuclide	Half-life [min]	Use in PET
^{11}C	20.4	Labelling of organic molecules
^{13}N	9.96	$^{13}NH_3$
^{15}O	2.03	$^{15}O_2$, $H_2{}^{15}O$, $C^{15}O$, $C^{15}O_2$
^{18}F	109.8	[^{18}F]-DG, ^{18}F
^{68}Ga	68.3	[^{68}Ga]-EDTA, [^{68}Ga]-PTSM, [^{68}Ga]-DOTA
^{82}Rb	1.25	Generator-produced perfusion tracer

Table 1.1: some commonly used radionuclides.

There is an abundance of radiotracers (^{18}FDG, $H_2{}^{15}O$, $^{13}NH_3$, ^{82}Rb…), some of which can be synthetized on-site without the need of a cyclotron, such as ^{82}Rb-chloride, which with a half-life of 76 seconds is increasingly used as a blood flow marker due to recent improvements in the image quality (Flotats et al. 2012). It has been proven that this tracer provides blood flow information in the myocardium similar to the one obtained with $^{13}NH_3$ (Yoshida et al. 1996) and has recently been used as a renal imaging agent (Tahari et al. 2014). ^{18}FDG has been extensively used as a tracer to measure metabolic rates (Huang et al. 1980) and $H_2{}^{15}O$ for blood flow quantification (Hermansen et al. 1998). While it is not the main purpose of this manuscript to make a thorough review of all the possible uses of the different available tracers, it is important to note that the choice of one over another is sometimes a complex decision in which a number of factors (binding potential, type of measurement, availability, half-life...) need to be taken into consideration.

The annihilation phenomenon causes the emission of two antiparallel 511 keV gamma photons that will be detected by the surrounding detectors from the PET system. Due to the momentum of the positron, the gamma photons may not form an angle of exactly 180º. The distribution of deviation angles around the 180º value is Gaussian with a standard deviation of 0.25º (Rahmim & Zaidi 2008). When both photons hit the detectors in coincidence within a certain time-window, a line of response (LOR) is generated. The whole process is depicted in Figure 1.1.

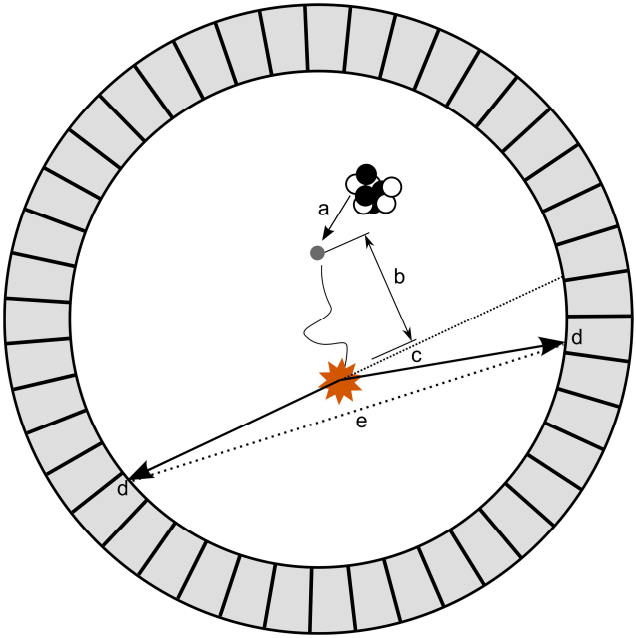

Figure 1.1: a positron is emitted due to nuclear decay processes (a) and interacts with the surrounding matter (b) until it reaches an equilibrium status and collides with an electron, producing two gamma rays (c). Due to the momentum of the previous movement, these rays may not form exactly 180º (dotted line); it is also possible that one or both of the photons suffer some form of scatter and deviate further from their original trajectories. Both rays interact with the detectors (d) and produce a line of response (e).

The list of coincidence events stored by the PET scanner transformed into a sinogram. Sinograms are the basis of most of the image reconstruction algorithms and consist on projections of the recovered coincidences along a given angle, from 0º to 180º.

Consider Figure 1.2, which shows the sinogram projection for a given study. For instance, a tumoral lesion appearing as a bright point in the reconstructed image has a sinusoidal trajectory on the sinogram projection, hence its name.

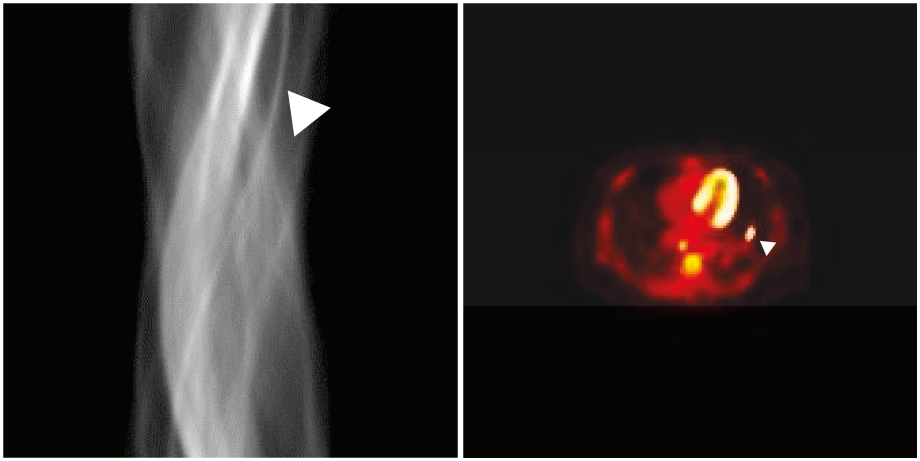

Figure 1.2: (Left) Sinogram from a single slice from a thorax acquisition study with ^{18}FDG. (right). Slice reconstruction from the previous sinogram. The white triangle pinpoints the location of a tumoral lesion both in the sinogram and the reconstructed image. It can be clearly seen that this point-shaped lesion traces a sinusoidal trajectory. Image courtesy of Cristina Chavarrías.

There are different algorithms used to obtain the reconstructed images from the sinogram. For an in-deep review of them, please refer to (Tong et al. 2010). Briefly, the PET image reconstruction process involves obtaining three distinct datasets: the emission data to be reconstructed, a set of normalization sinograms to correct for different detector efficiencies (a "blank scan") and the photon attenuation behavior of the object. This last dataset can be obtained using and external radiation source that transmits ("transmission scan") photons through the body to the detector or combining the CT information in PET/CT systems. With these three distinct datasets the final image can be reconstructed.

However, there are a number of sources of uncertainty that affect the mathematical computation done to locate the exact line of response. The most important effects are (Rahmim & Zaidi 2008; Tong et al. 2010):

- Emitted positrons travel a certain distance before the annihilation event takes place (Figure 1.1). This distance, known as the positron range, depends on the energy distribution of the positron-emitting isotope. As a consequence, the response line is generated not on the place where the positron was emitted, but within a certain distance from that point.
- As shown before, the gamma photons do not form exactly 180º due to the momentum of the positron at the moment of the annihilation event. About 1.54 – 1.76 mm FWHM blurring can be expected from this phenomenon in a typical whole-body

scanner (Rahmim & Zaidi 2008), or around 0.17 mm for animal scanners, since this blurring effect depends on the diameter of the detector ring.

- The scattering events produced by the interactions between the gamma photons and the surrounding matter after the annihilation may cause a change in the trajectory of one or both of them. Based on this, we can divide the valid coincidence events registered by the system in:
    - True: none of the photons are scattered. They collide with the detectors following their original trajectories.
    - Scatter: one or both of the photons are scattered and the resulting line of response differs from the original trajectory.
- Random coincidences may also take place. The trajectories of the gamma rays from two independent annihilation events take directions in such a way that only one photon from each interaction hit the detectors in time coincidence. The resulting line of response is completely uncorrelated with the distribution of the tracer.

As a consequence of all these previous effects, there is a minimum of spatial resolution to expect from any PET image. Because of this finite spatial resolution, a small photon source will appear larger and dimmer in the reconstructed image (Soret et al. 2007) and part of its activity will fall outside its "natural" limits. See Figure 1.3 for a graphical representation of this effect, which mathematically is the result of convolving the true representation of the object with the point-spread function (PSF) of the system.

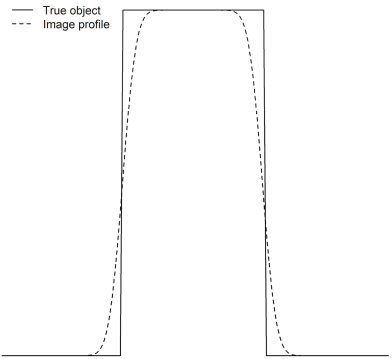

Figure 1.3: finite resolution effect on a point source.

Also, as the image is discretized in a series of voxels within the image matrix, the intensity level of a given voxel will be a function of all the different tissues included in it, as the matrix divisions obviously do not follow the activity distribution within the organ under study. This tissue mixing within the same voxel is known as the partial volume effect (PVE).

The practical consequence of the PVE and the blurring in general is that small regions surrounded by a cold background (that is, with little or no activity) appear bigger and with a lower activity concentration due to spill-out to adjacent regions. Conversely, a cold region surrounded by tissues with high activity will show higher activity concentrations due to spill-in from the hot neighboring regions.

Therefore, the accurate image segmentation that is required for a correct quantification of the regional activities becomes challenged unless the PVE can be corrected or minimized during the segmentation process.

1.2 Dynamic PET and kinetic modeling

Though it is common to study biological parameters from a single, static image acquisition, the inclusion of the time factor and the development of kinetic models allow improving the information that can be extracted regarding the organ or tissue uptake and metabolism. This approach models each organ as a response defined by its relationship with the amount of tracer being offered by the system (input function). Mathematically, this problem is solved using models that try to approximate the actual biological mechanisms that influence the tracer uptake inside the organ.

The radioactivity concentration in a tissue after the tracer injection depends primarily on the tissue physiology and the tracer input function, that is, the time-course changes of the tracer being offered to the organ via blood or plasma (Bailey et al. 2003). With the tissue TAC, along with a measurement of the input function obtained either via blood sampling of using a surrogate of it like the image-derived input function (Schroeder et al. 2007; Xiong et al. 2012; Tantawy & Peterson 2010; de Geus-Oei et al. 2006) it is possible to estimate physiological parameters such as blood flow (Lortie et al. 2007) or glucose metabolism (Huisman et al. 2012).

The key assumptions taken for granted regarding the behavior of the tracer are (Morris et al. 2004):

1. The amount of tracer injected is a true trace amount. That is, it does not produce any change whatsoever in the physiology of the organ that is being studied.
2. The tracer and the molecule it wants to emulate (the *tracee*) are in a steady equilibrium state and share the same dynamics: the tracer goes wherever the tracee goes.

3. The act of labeling the tracer molecule does not alter its properties.

To analyze these studies, we can distinguish between data-driven and model-driven techniques (Gunn et al. 2002). The difference is that the latter make assumptions regarding a compartmental structure that is used to describe the behavior of the tracer and try to estimate the system parameters. This thesis is centered on the use of those compartmental models.

1.2.1 Compartmental models

Here, the term compartment makes reference to a physiologically independent pool of tracer. The number of compartments depends on the physiological and biochemical properties of the tissue or organ under study (Gunn et al. 2001), and the characterization of a certain tracer often involves establishing the number of compartments that best model its behavior.

Quantification of this type of studies involves analyzing the changes in the compartment tracer concentration on each relevant organ or tissue. These can be described using the blood tracer concentration (the input function, the amount of tracer available in the system at any given time) and the exchange rate constants that describe the amount of tracer that are exchanged between the different compartments (Figure 1.4).

As the input function is measured, it is not considered a compartment in the mathematical sense, though it may very well be considered one physiologically. In some reference texts, it is treated and displayed like just another compartment, but some authors ((Morris et al. 2004) for instance) warn the reader: "[…] the input concentration is often depicted as a box in graphical representations of kinetic models. We will adhere to this custom, but the reader should be aware that it is not strictly correct." In this thesis the non-compartment convention will be used and the arterial tracer concentration will be depicted in a way that shows its distinct nature.

The relationship between the tracer exchange among the different compartments is described using differential equations (see next section). In order to solve these differential equations, another assumption must be made regarding the initial state of the system. In this case, the initial conditions must be zero: there is no tracer present in the system prior to the injection time. Also, it is assumed that the same input function is seen by all the organs, which is not true at the subject level as a whole, but it can be assumed true at organ or tissue level. This input function is the measured radioactivity in the blood plasma.

In general, in order to avoid quantification errors, the acquired data must be inspected for the correctness of certain features such as the presence of minimal or no counts in the first frame, as said before, the correct acquisition of the bolus first pass (peak clearly acquired), the presence of enough counts in the frames showing the tissue uptake and the clearance of tracer concentration in blood (Case & Bateman 2013).

As both the input function and the tissue activity are known, the rate parameters can be fitted from the measured data using a non-linear least squares method such as Gauss-Newton, Levenberg-Marquardt or Powell, to cite just a few.

In the following subsections, the most common models will be presented in order to introduce the mathematical foundations behind this process.

1.2.1.1 One-tissue compartment model

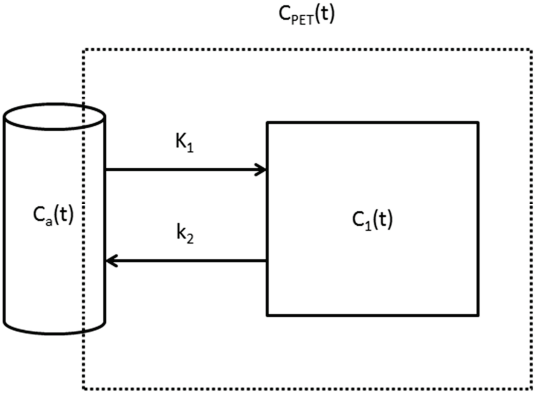

Figure 1.4: diagram of the one-compartment model.

In this simple model, a single differential equation describes the behavior of the tracer using the blood tracer concentration $C_a(t)$, the two unidirectional rate constants K_1 and k_2 and the compartmental tracer concentration $C_1(t)$.

$$\frac{dC_1(t)}{dt} = K_1 \cdot C_a(t) - k_2 \cdot C_1(t) \tag{1.1}$$

The above differential equation can be easily solved to

$$C_1(t) = K_1 \cdot e^{-k_2 t} \otimes C_a(t) \tag{1.2}$$

Equation (1.2) can be interpreted as the impulse response of the tissue to the input function. As the tissue signal includes a fraction of the blood activity due to the tracer activity in the intravascular space, a blood fraction correction has to be made. Typically, the final equation that needs to be solved is given by

$$C_{PET}(t) = (1 - v_B) \cdot C_1(t) + v_B \cdot C_a(t) \tag{1.3}$$

where the term v_B is the fraction of blood in tissue.

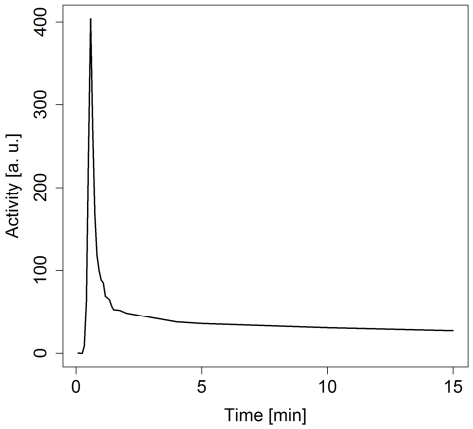

Figure 1.5: input function signal obtained from the manual segmentation of the left ventricle of a swine $^{13}NH_3$ study.

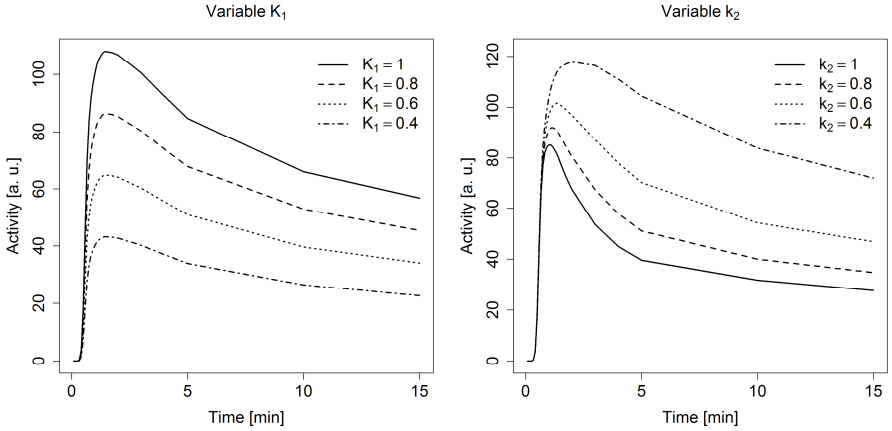

Figure 1.6: influence of different K_1 (left) and k_2 (right) values on the tissue model. Intuitively, K_1 controls the initial curve amplitude and k_2 the decay rate. The fixed parameter always takes a value of 0.5. The fraction of blood in tissue for this simulation is 0.

The TAC shown in Figure 1.5 has been used to generate the tissue simulations shown in Figure 1.6, where the effect of the two rate parameters on the tissue TAC shape can be evaluated using Equation 1.2.

1.2.1.2 Reversible two-tissue compartment model

Another, more complicated model consists of two compartments. A typical tracer to which this model is applied is ^{18}FDG. In this case, the tracer is extracted from the arterial plasma into the first compartment (K_1, non-displaceable tracer) and is metabolized into the mitochondria to FDG-6-PO4 by the hexokinase enzyme into the second compartment (k_3, specifically bound or metabolized tracer). If the study takes longer than one hour, dephosphorylation of FDG occurs (k_4). As can be seen, the number of compartments must match the expected biological activity for the tracer or the molecule it is attached to. A graphical representation of a general two-tissue compartmental model can be seen in Figure 1.7.

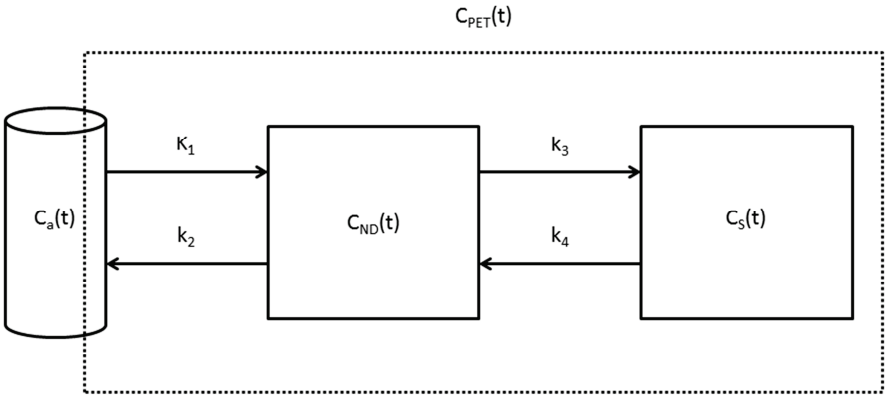

Figure 1.7: diagram of the reversible two-tissue compartment model. The different compartments represent the non-displaceable $C_{ND}(t)$ and specifically bound $C_S(t)$ tracer. The input function is represented by $C_a(t)$. The signal measured by the PET system includes both compartments plus a fraction of blood activity $C_{PET}(t)$.

The differential equations that describe the relations between the compartments can be obtained just like in the one compartment case (Zaidi 2005):

$$\begin{aligned} \frac{dC_{ND}(t)}{dt} &= K_1 \cdot C_a(t) - (k_2 + k_3) \cdot C_{ND}(t) + k_4 \cdot C_S(t) \\ \frac{dC_S(t)}{dt} &= k_3 \cdot C_{ND}(t) - k_4 \cdot C_S(t) \end{aligned} \tag{1.4}$$

Solving the above equations yields:

$$C_{ND}(t) = \frac{K_1}{\alpha_2 - \alpha_1}[(k_4 - \alpha_1)e^{-\alpha_1 \cdot t} + (\alpha_2 - k_4)e^{-\alpha_2 \cdot t}] \otimes C_a(t)$$
$$C_S(t) = \frac{K_1 \cdot k_3}{\alpha_2 - \alpha_1}[e^{-\alpha_1 \cdot t} - e^{-\alpha_2 \cdot t}] \otimes C_a(t) \quad (1.5)$$

Where

$$\alpha_1 = \frac{k_2 + k_3 + k_4 - \sqrt{(k_2 + k_3 + k_4)^2 - 4 \cdot k_2 \cdot k_4}}{2}$$
$$\alpha_2 = \frac{k_2 + k_3 + k_4 + \sqrt{(k_2 + k_3 + k_4)^2 - 4 \cdot k_2 \cdot k_4}}{2} \quad (1.6)$$

As in the previous case, the tissue signal obtained from a ROI on the image will consist on the "pure" tissue activity plus a fraction of blood that has to be corrected with another parameter to obtain accurate estimates for the kinetic parameters:

$$C_{PET}(t) = C_{ND}(t) + C_S(t) + k_5 \cdot C_a(t) \quad (1.7)$$

Equation (1.7) uses the terminology from (Zaidi 2005), where the blood fraction correction factor is named like the rest of the kinetic parameters. The PMOD software package (PMOD Technologies Ltd, Zurich, Switzerland), as well as other references (Morris et al. 2004), use a slightly different approach and terminology for this correction which will be the one used in this thesis and that matches more closely Equation (1.3):

$$C_{PET}(t) = (1 - v_B) \cdot (C_{ND}(t) + C_S(t)) + v_B \cdot C_a(t) \quad (1.8)$$

Equation (1.8) instead of (1.7) reinforces the concept that v_B is a fraction of the total signal, not just a scale factor.

In the above equations, K_1 is the plasma to tissue rate constant and typically has units of $ml \cdot g^{-1} \cdot min^{-1}$ or $ml \cdot cm^{-3} \cdot min^{-1}$, while the k_2, k_3 and k_4 rate constants have units of min^{-1}. K_1 is distinguished in upper case to denote that its units are different from the other rate constants.

In this work we are following as closely as possible the terminology laid out in (Innis et al. 2007) regarding the names of the two compartments (non-displaceable and specifically bound), but in other places the different compartments may receive other names (such as simply the "bound" compartment for the second compartment, of "free tracer" for the first one).

Figure 1.8 shows how the different parameters affect the shape of the model. The input function from Figure 1.5 has also been used to build the different TACs.

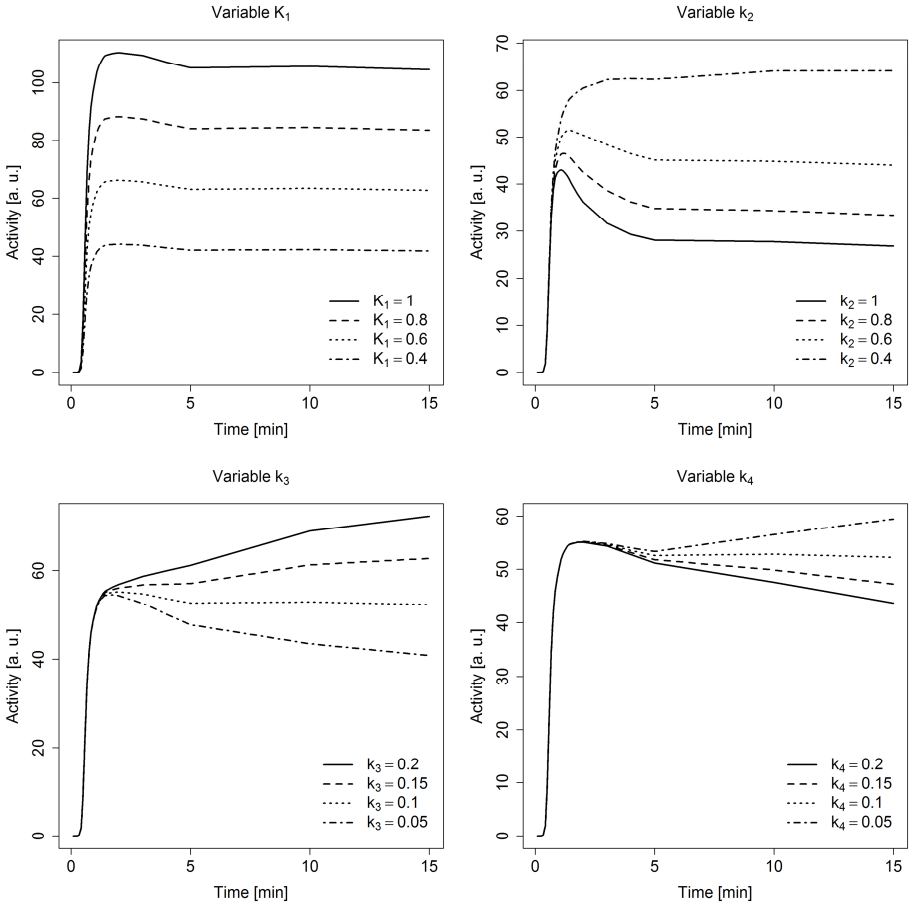

Figure 1.8: influence of the different rate parameters on the compartmental model. When fixed, the parameters have values of 0.5 for K_1 and k_2 and 0.1 for k_3 and k_4. The blood fraction in tissue has been set to 0 to build these models.

1.2.1.3 Irreversible two-tissue compartment model

The above equations describe the behavior of a reversible tracer such as the ^{18}FDG for studies taking longer than one hour. For $^{13}NH_3$ or short ^{18}FDG studies, the k_4 constant is zero, as the tracer is irreversibly trapped in the specifically bound compartment and there is no tracer

exchange back between the second and the first compartment (Figure 1.9). In the case of $^{13}NH_3$, if short acquisition times have been used (about five minutes), a 1-tissue compartmental model may be used for this tracer (DeGrado et al. 1996).

The equations that define this system can be obtained by simplifying the previous equations when $k_4 = 0$. The exact formulation is given in the following lines.

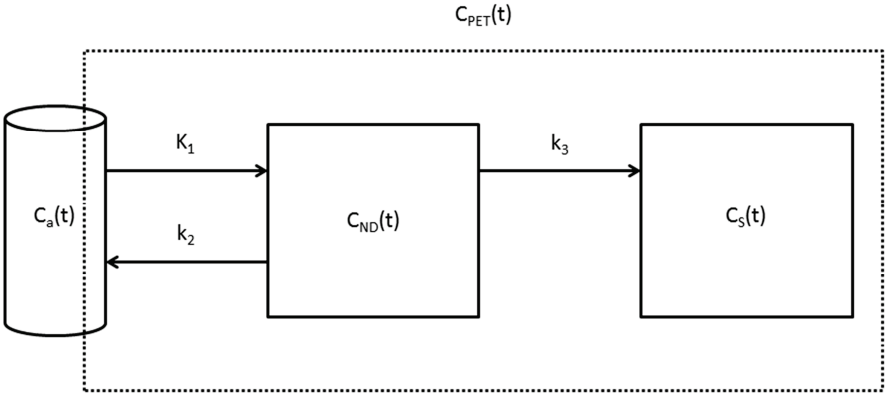

Figure 1.9: diagram for the irreversible two-tissue compartment model. The compartments have been labeled just like in the previous case. Note that in this case there is no back tracer exchange between the two compartments ($k_4 = 0$).

The differential equations that define the tracer exchange between both compartments are solved by the following expression:

$$C_{ND}(t) + C_S(t) = \left(\frac{K_1 k_2}{k_2 + k_3} e^{-(k_2 + k_3)t} + \frac{K_1 k_3}{k_2 + k_3}\right) \otimes C_a(t) \tag{1.9}$$

As in previous cases, it is necessary to compensate the residual fraction of blood in the tissue activity, thus:

$$C_{PET}(t) = (1 - v_B) \cdot (C_{ND}(t) + C_S(t)) + v_B \cdot C_a(t) \tag{1.10}$$

1.2.1.4 Volumes of distribution

The term *volume of distribution*, in most imaging studies, makes reference to the ratio of tracer in tissue to that in plasma (Innis et al. 2007). As explained before, a certain tissue may contain non-displaceable plus specifically bound tracer. The first compartment can be further divided

into free tracer (in the tissue water) and nonspecifically bound. Therefore, the total volume of distribution inside the tissue is given by the following equation:

$$V_T = V_{ND} + V_S \tag{1.11}$$

These kinetic parameters can be easily computed from the rate parameters obtained from the different kinetic models.

For the one-tissue compartment model, the total volume of distribution is simply

$$V_T = \frac{K_1}{k_2} \tag{1.12}$$

Whereas for the reversible two-tissue compartment model this becomes

$$V_T = \frac{K_1}{k_2}(1 + \frac{k_3}{k_4}) \tag{1.13}$$

$$V_{ND} = \frac{K_1}{k_2} \tag{1.14}$$

The volume for the specifically bound tracer fraction can then be computed by subtracting Equation (1.13) and (1.14).

1.2.1.5 Net uptake

When there is irreversible trapping in the model, a compound rate parameter commonly used is the tracer net uptake into the irreversibly bound compartment (Bailey et al. 2003). This parameter is denoted by K_i and can be easily obtained from the individual rate parameters as

$$K_i = \frac{K_1 k_3}{k_2 + k_3} \tag{1.15}$$

In the case of studies that involve ^{18}FDG, for instance, this parameter is closely related to the tissue glucose metabolic rate, which is given by the following equation

$$MRGlu = \frac{C_{glu}}{LC} \cdot K_i \tag{1.16}$$

where C_{glu} is the glucose concentration in blood and *LC* is the *lumped constant*, which the ratio of the volumes of distribution of ^{18}FDG and glucose multiplied by the hexokinase phosphorylation ratio for the two hexoses (Spence et al. 1998).

1.2.2 Linear approximations

As can be seen in the previous sections, the mathematical solutions increase in complexity as more compartments and their corresponding tracer exchange rates are added to the system. Furthermore, non-linear least squares has several problems, the main ones being that it is slow, depends on an initial guess (Kimura et al. 2007; Ichise et al. 2002) and the errors for the individual rate parameters then to be high. As in many cases the clinical diagnosis can be done using not only the isolated rate exchange constants but on a physiologically meaningful combination of them, such as the volume of distribution, there are several linear approximations. These most commonly used linear approximations are also known as graphical methods, as they rely on the relationship that appears between the input function and the tissue curve when they are plotted in a certain way.

Furthermore, these linear approximations have the advantage of being fast to compute, allowing them to be used in the generation of parametric maps (static 3D images) that show the spatial distribution of the combined parameter.

In the following sections two of the most common linear approximations will be detailed: the Patlak plot and the Logan plot, and some equations that try to improve them by minimizing the effect of the signal noise on the obtained fitting terms.

1.2.2.1 Patlak plot

The Patlak plot (Patlak et al. 1983) is used for irreversible two-tissue compartment models. It can be observed that rearranging the compartmental model equation can yield the following expression:

$$\frac{C_{PET}(t)}{C_a(t)} = \frac{K_1 k_2}{(k_2 + k_3)^2} + \frac{K_1 k_3}{k_2 + k_3} \frac{\int_0^t C_a(s)ds}{C_a} \tag{1.17}$$

In this case, the system can be solved using linear least square methods, which are much faster than non-linear ones and can be used, for instance, for the generation of parametric maps. It can be observed that the slope term is equal to the K_i parameter detailed in the previous section (Equation (1.15)).

It has to be taken into account that the Patlak plot (and this is also applicable to the Logan plot) is valid for $t > t^*$, that is, for a time t for which the system is in equilibrium. It is important to find that optimal point and to check that indeed the plot is linear in that segment, or the slope

will be overestimated. Furthermore, this formulation allows the intercept term to be interpreted as the volume of distribution.

Figure 1.10 shows the Patlak regression for a dataset consisting on the left ventricle TAC taken as the input function and the myocardium TAC for swine $^{13}NH_3$ study. The detection of the $t < t^*$ point has been automatically made by selecting only those points that offered a regression with less than 10% maximum residual error value. This is the approach used by the PMOD imaging analysis platform.

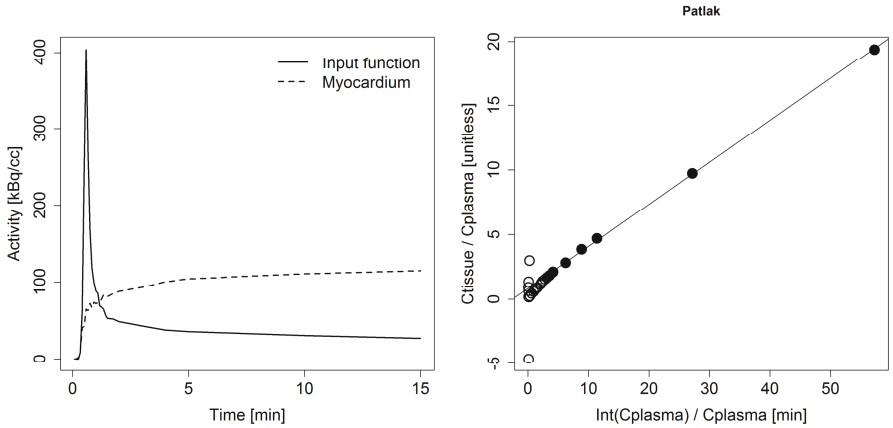

Figure 1.10: Left: two time-activity curves from the input function (straight line) and myocardium (dotted line) from a $^{13}NH_3$ swine study. Right: Patlak analysis for the previous curves. White dots represent the time points before the equilibrium point is reached ($t < t^*$). Only filled dots are used for the regression. The selection of the optimal points has been made with the 10% threshold, as the PMOD software package proposes.

1.2.2.2 Logan plot

The Logan plot (Logan et al. 1990) is used for reversible two-tissue compartment models to obtain the total volume of distribution for the tissue being studied. In a way analogous to the Patlak plot, rearranging the compartmental model equations gives:

$$\frac{\int_0^t C_{PET}(s)ds}{C_{PET}} = -\frac{k_2 + k_3 + k_4}{k_2 k_4} + \frac{K_1}{k_2}\frac{k_3 + k_4}{k_4}\frac{\int_0^t C_a(s)ds}{C_{PET}} \tag{1.18}$$

In the previous equation, the slope is equal to the total volume of distribution, as detailed in Equation (1.13).

Figure 1.11 shows the result of a Logan regression to obtain the volume of distribution from a mice study using a ^{68}Ga-DOTA based tracer.

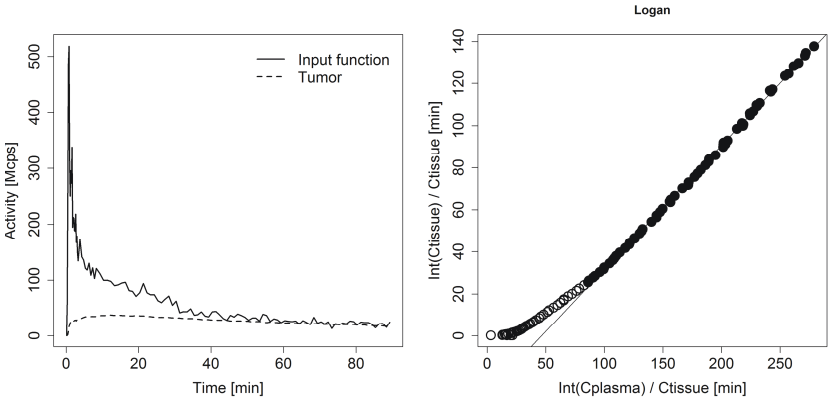

Figure 1.11: (Left) Input function from the myocardium region and tumor TAC obtained from a mice study using a ^{68}Ga-DOTA based tracer. (Right) Logan regression for said study. As in the Patlak example, not all the points have been used for the regression process. The optimal time $t > t^*$ has also been obtained automatically using the 10% maximum error approach.

1.2.2.3 Multilinear variations

With all their simplicity and widespread use, the Patlak and Logan methods are not without their faults. For instance, both require a precise identification of the point from which the plot becomes linear. This can lead to small divergences in the final result, depending on the algorithm used to choose that precise time point. PMOD computes the point from which the linear regression has an absolute error smaller than 10% for each fitted point, while other papers set a specific time point depending on the tracer if its kinetic behavior is known. Furthermore, as the tissue data is generally considered to be noisier than the input function, some effort has been made into rearranging the equations so that this data only appears as the dependent term of the linear equation in order to achieve smaller uncertainties in the parameter estimation after the fitting process. The two main works that deal with this approximations are (Ichise et al. 2002) and (Kim et al. 2008) and can be used as replacements for the Logan and Patlak methods.

The first of the referenced works proposes the following formulations as an alternative to Logan (known as MA1 and MA2):

$$C(T) = -\frac{V}{b}\int_0^T C_p(t)dt + \frac{1}{b}\int_0^T C(t)dt \tag{1.19}$$

$$C(T) = \gamma_1 \int_0^T \int_0^s C_p(t)dtds + \gamma_2 \int_0^T \int_0^s C(t)dtds + \gamma_3 \int_0^T C(t)dt + \gamma_4 \int_0^T C_p(t) \quad (1.20)$$

In the previous equation, $\gamma_1 = k_2 k_4 V_T$, $\gamma_2 = -k_2 k_4$, $\gamma_3 = -(k_2 + k_3 + k_4)$, $\gamma_4 = K_1$. The time-dependent activities C and C_p refer to the tissue curve and the input function curve, respectively. While the first equation is more robust regarding the noise influence, it still needs to compute the optimal time point $T > t^*$. The second equation reorders the terms so that this is not necessary and the final V and V_S values can be computed using the γ parameters and the whole TAC information.

In a similar fashion, (Kim et al. 2008) proposes the following equations as a replacement for the Patlak linear regression (MLAIR1 and MLAIR2, respectively):

$$C_T(t) = P_1 C_a(t) + P_2 \int_0^t C_a(\tau)d\tau + P_3 \int_0^t C_T(\tau) + P_4 \int_0^t \int_0^\tau C_a(s)dsd\tau \quad (1.21)$$

$$\int_0^t C_T(\tau)d\tau = P_1' \int_0^t \int_0^\tau C_a(s)dsd\tau + P_2' \int_0^t C_a(\tau)d\tau + P_3' C_a(t) + P_4' C_T(t) \quad (1.22)$$

In Equation (1.21), K_i is given by $-P_4/P_3$. In Equation (1.22), K_i is given directly by P_1'; the other P values contain other combinations of the individual rate parameters. In this case, both equations have been arranged so that it is not necessary to compute the optimal t time point, thought Equation (1.22) yielded considerably smaller errors in empirical tests. In these equations, C_T and C_a refer to the tissue TAC and the input function, respectively. This method, along with the classical Patlak equation, has been used to generate the data shown in Figure 1.12. The image shows how this approach yields results that are much more robust with regards to noise distortions.

These multilinear approaches can even be used to extract the individual rate parameters from the partial regression constants (the P values from Equation (1.21) or (1.22), for instance). While this is a faster solution than using a non-linear fit, the resulting errors for the individual rate parameters are bigger (Ikoma et al. 2008) and this particular approach is not widely used in the literature.

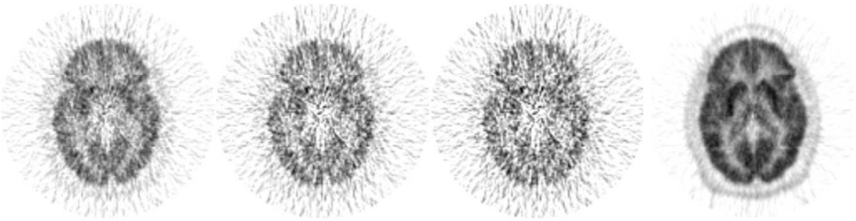

Figure 1.12: example of three parametric Patlak maps (three leftmost images, each with a different t) and the parametric map obtained using Equation (1.22). This image shows both how the selection of the optimal equilibrium time point t* affects the K_i computation, and how the multilinear approach is much more robust. Image modified from* (Kim et al. 2008).

1.3 Automatic segmentation methods: a review

As seen in the previous section, compartmental analysis makes several assumptions regarding the tracer distribution within the different organs. For this particular problem of segmentation, it is important to notice that individual organ TACs should be homogeneous. That is, each organ is defined by a TAC that contains all the information regarding the uptake of that organ, trying to minimize as much as possible any kind of mixing with the surrounding organs or tissues due to partial volume effects (Maroy et al. 2010). Otherwise, the rate parameters obtained will not describe precisely the kinetics of the organ under study.

As explained before, due to the image reconstruction process not being perfect, the system response function for a single activity point is bell-shaped (Zaidi 2005) and part of its activity dilutes in the background. In an analogous way, the activities from two close objects will be mixed, producing two differentiated effects: *spill-over* and *spill-in*. The first term makes reference to the mixture of different activities when a high activity region loses activity in the surrounding, lower-activity tissues; the second refers to the contrary phenomenon: an initially low activity tissue receives it from an adjacent, high-activity region.

Typically, tissue TACs are extracted by an experienced operator. The process involves the manual and careful delineation of the organ while trying to stay away from the edges; in some cases, an anatomical image (like that offered by a CT study) is used in the manual segmentation process. It is also common to use a static PET image generated from the sum of all the study frames, or just some the first or last ones, depending on the type or data that is desired. For instance, in a cardiac study, an operator might want to get a summed image containing only the first frames in order to locate the input function region (left ventricle in most cases), and a later frames image to locate the myocardium tissue; it is also possible to produce another image that subtracts the later one from the first one in order to minimize the spill-in from the myocardium into the last points of the input function. Examples of the images that can be generated during this process are shown on Figure 1.13.

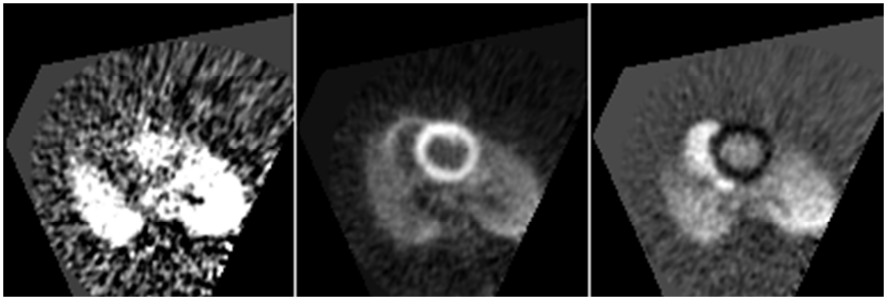

Figure 1.13: set of images generated for obtaining the input function from the left ventricle in a swine cardiac study with $^{13}NH_3$ as tracer using a manual segmentation process. Left: averaged image of the first 8 frames of the study, in which the tracer enters the body and it is shown in the left ventricles and the lungs. Center: averaged image of the last 4 frames of the study, with the myocardium showing high uptake levels. Right: the subtraction of the previous two images. It shows the left ventricle surrounded by the area into which the myocardium is more prominent. Note the difference between this image and the leftmost one in terms of the enhancement of the delineation limits.

However, this procedure has great inter and intra-operator variability (Dewalle-Vignion et al. 2011) and is time-consuming, and difficult to replicate (Wong et al. 2002; Zanotti-Fregonara et al. 2009). Furthermore, the obtained TACs may consist of a mixture between the actual tissue TAC and the surrounding regions if they are not far enough from the adjacent organs and even the precise location of the ROI (for instance, in the case of human heart studies) has a non-negligible influence in the final result (Bacharach & Carson 2013; Zanotti-Fregonara et al. 2011; Vasquez et al. 2013). Also, a region that appears as homogeneous in the CT image, if that is the imaging modality being used for the segmentation, may present different kinetic behaviors due to necrosis, as in the case of tumoral regions (see Chapter 6 for an example) and several different regions will be grouped into a single one, creating a bias in the kinetic model, that usually expects a homogeneous behavior in the supplied tissue TAC.

Due to all these problems, there is a very fertile research area in the development of new automatic or semi-automatic segmentation algorithms. In the field of dynamic PET segmentation, several different methods have been proposed, including principal component analysis (Pedersen et al. 1994), k-means clustering (Wong et al. 2002), factor analysis (Klein et al. 2008; El Fakhri et al. 2005; Sitek et al. 2002), hierarchical clustering (Guo et al. 2003; Liptrot et al. 2004), segmentation based on TAC similarity metrics (Brankov et al. 2003; Maroy et al. 2008; Maroy et al. 2010), independent component analysis (Magadán-Méndez et al. 2010), multi-modality techniques to estimate the image-derived input function (Fung & Carson 2013) and approaches based on spectral clustering (Mouysset et al. 2013), to cite just a few.

These algorithms aim at resolving, in general, the problem of variability of the manual segmentations. Some of these methods suffer from region superposition: several voxels may

belong to more than one tissue at once, as is the case of the factor analysis. Some the previously cited works use this method as a first approach and in a second step try to find a minimization of this superposition (El Fakhri et al. 2005; Sitek et al. 2002). In any case, it needs to be noted that the purpose of these segmentations is not the visual separation of the different image areas, but the extraction of well-defined TACs that describe the kinetic behavior of each tissue in a way that is reproducible and minimizes *spill-over* effects. To differentiate this process from the common segmentation based on anatomical features, sometimes this TAC extraction process is referred to as *functional segmentation* (Rousset et al. 1998; Parker 2005).

As can be seen from the previous references, most publications currently available aimed at solving this particular problem involve the use of unsupervised machine learning techniques or clustering algorithms, with very few exceptions (Turkheimer et al. 2007). Other imaging segmentation problems can be solved using supervised machine learning algorithms, and there are specific imaging processing libraries published, such as the Trainable Weka Segmentation ImageJ Plugin (Arganda-Carreras et al. 2013) that uses the Weka machine learning libraries (Hall et al. 2009). In the case of the segmentation of dynamic studies, supervised approaches have not been widely developed, probably due to the great data variability found in dynamic PET studies (TACs depend on the tracer, the type of injection, the specific acquisition times and tissues being measured…). In this work we show that, though in a limited way and only as a proof of concept, it is possible to use supervised techniques for sets of studies that have similar kinetic properties (Chapter 3).

In the following sections we briefly explain some of the most common methods used for automatically segmenting dynamic nuclear studies along with some proposals from this PhD thesis.

1.3.1 k-means

K-means is one of the most useful clustering algorithms and one of the most used in many different fields due to its conceptual simplicity and the easy interpretation of its results. It has been applied successfully in solving the functional segmentation problem, either as a complete solution by itself or as a first step component inside a more elaborated pipeline (Jinman Kim et al. 2006; Zheng et al. 2011; Liptrot et al. 2004; Wong et al. 2002).

This algorithm works in the following way:

1. The user sets k different clusters to be initialized. This initialization is done by selecting k random TACs from the image. A maximum number of iterations is also set here. This is done because this algorithm is guaranteed to converge, but it may take too long to do so; in practice, few iterations are needed and this limit is seldom reached.

2. For each TAC in the image, compute the distance to each of the cluster centroids. The TAC is labeled with the centroid with the shortest distance.
3. Compute new centroids using labels set in the previous step.
4. Repeat steps 2 and 3 until there is no change in the new centroids computed or until the maximum number of iterations has been reached.

Typically, the Euclidean distance is used, but other metrics are possible (correlation, cosine, Mahalanobis).

The two most important limitations of this method are the number of clusters and the random initialization (see Figure 1.14). Both are usually addressed by running the algorithm several times on the same data with different initial clusters and then choosing the most correct partition by some defined criterion (such as the intraclass correlation coefficient, or the Akaike Information Criterion, for instance). This might lead nonetheless to sub-optimal segmentations and generally causes this algorithm to generate non-repeatable segmentations unless a deterministic initialization can be used. Some developments have been made in this sense (Arthur & Vassilvitskii 2007), though they have not been applied to the dynamic PET segmentation problem to the extent of our knowledge.

Figure 1.14: three different k-means segmentations on the same image (k = 5). The result is different each time and the number of clusters should be higher, as several as the different regions are not clearly delimited.

1.3.2 Leader-follower

A family of clustering algorithms called *on-line clustering techniques* does not make any assumption regarding the number of clusters that are needed to partition a certain sample (Duda et al. 2001). In the case of dynamic nuclear medical images this approach can be employed due to the lack of information regarding the number of homogeneous organs or tissues in the field of view and the activities within them, which in many cases might be heterogeneous due to mixing of different organs caused by partial volume effects.

These algorithms can be thought of like an inverse version of k-means. Instead of setting a predefined number of clusters, a threshold is set and the algorithm creates new clusters as needed. The inclusion of each new voxel in a given cluster modifies its centroid, so every single cluster contains, at a given point in time, a representation of all the TACs included in it. These algorithms do not need to be iterative and are able to finish the clustering process with a single pass through the dataset. These algorithms are very sensitive to the order in which the voxels are analyzed, but this aspect can be controlled to offer clustering results that take into consideration the loss of amplitude from a hot region into a cold background characteristic of dynamic PET studies.

As far as we know, an algorithm of this kind has not been applied to this particular problem of segmentation and TAC extraction, despite its potential applications. In this PhD thesis we propose an open implementation of a leader-follower algorithm under ImageJ and validate it using rodent studies (Chapter 6).

1.3.3 Principal Component Analysis

Principal component analysis (PCA) has been used typically to reduce the dimensionality of a dataset and understand which variables are the most descriptive of the dataset variance by providing a sequence of best linear approximations (Hastie et al. 2009). The principal components consist of uncorrelated projections of the data ordered by the amount of variance explained. When using PCA to reduce the dimensionality of a given dataset, it is common to keep only those projections that explain a certain amount of variance (for instance, 95%).

Mathematically, the PCA computation involves splitting the data using Singular Value Decomposition (SVD). Consider the matrix **X**, which is an *Nxp* matrix (in the case or our images, they are unfolded to form the *N* voxels times *p* time points 2D structure) which has been previously centered (the mean value for each column has been subtracted). In that case, we can build the SVD in the following way:

$$\mathbf{X} = \mathbf{U}\mathbf{D}\mathbf{V}^T \tag{1.23}$$

In this case, the columns of the matrix **UD** are the principal components of **X**. In any case, it is computationally more efficient to compute PCA using the covariance matrix:

$$\mathbf{X}^T\mathbf{X} = \mathbf{W}\mathbf{D}^2\mathbf{W}^T \tag{1.24}$$

$\mathbf{X}^T\mathbf{X}$ forms the covariance matrix of **X** and is a *pxp* matrix, considerably smaller than the original one.

There is an excellent and in-depth explanation of the application of PCA to dynamic PET images in (Pedersen et al. 1994). In the area of image analysis, this transformation is also called the Karhunen-Loève transform or Hotelling transform.

Once the image has been converted into its principal component projections, these may contain the TACs that better describe certain organs or regions of the image. See for instance the projections shown in Figure 1.15.

While this method has been used in segmenting dynamic PET studies either as a preprocessing step or the final method (Pedersen et al. 1994; Razifar et al. 2009; Razifar et al. 2006), it is widely recognized that the principal component TACs may be mathematically correct but not physiologically correct. That is, they do not describe accurately the different TACs due to physical constraints (for instance, they show negative values). To overcome this problem, factor analysis (Barber 1980) was been proposed as a related TAC extraction technique. Factor analysis consists on performing a rotation on the principal components with positivity constraints (Wu et al. 1995) so that the resulting TACs are physiologically sound.

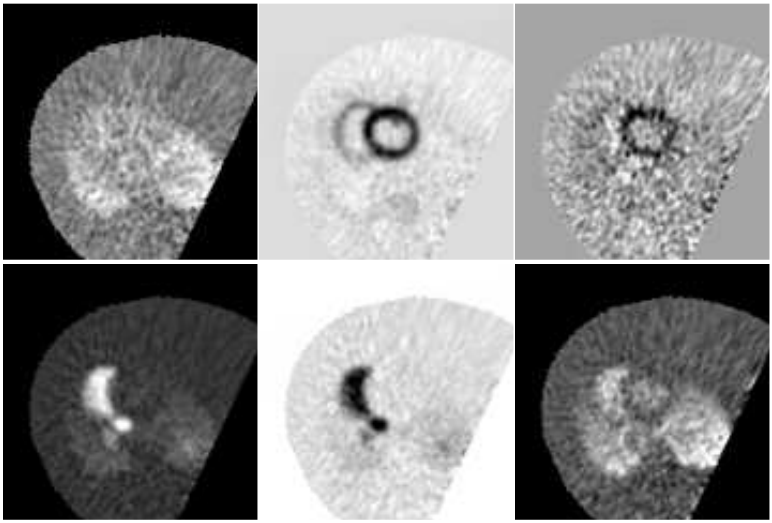

Figure 1.15: 6 PCA projections of the same cardiac study shown in Figure 1.13. It can be clearly seen how some projections highlight the different structures (myocardium, right and left ventricles, lungs) that are susceptible of being segmented by an operator.

One of the problems of factor analysis is that the solution is not unique, causing different factor images to overlap, and that the parameters for its computation are heavily dependent on the type of study being analyzed (El Fakhri et al. 2005). Also, as in the case of the k-means algorithm,

different executions of the algorithms yield different results. Research lines on this algorithm focuses on minimizing the overlapping between different regions (Sitek et al. 2002).

1.3.4 Independent Component Analysis

Independent component analysis (ICA) has been applied extensively in the field of signal processing, where it is used as a source separation algorithm (Hastie et al. 2009; Duda et al. 2001). In the simplest case, consider just two independent signals, $s_1(t)$ and $s_2(t)$. If they suffer from some kind of additive mixing, the following will be registered by the detector:

$$\begin{aligned} x_1(t) &= a_1 s_1(t) + b_1 s_2(t) \\ x_2(t) &= a_2 s_1(t) + b_2 s_2(t) \end{aligned} \tag{1.25}$$

In matrix form, we wish to recover the mixing matrix **A** in X = **A**S such that S = $\mathbf{A}^{\mathrm{T}}$X are independent (and non-Gaussian). This simple example can be seen in Figure 1.16.

ICA can be applied to dynamic studies just like any other previous algorithm: the 3D image is converted into a 2D matrix with the voxels in the rows and the time points in the columns, and the mixing matrix is obtained in order to extract the original, unmixed signals (Figure 1.17). It has been successfully applied to the problem of segmenting dynamic PET studies in some published works, but it has always been the same type of study (cardiac images) and tracer ($H_2{}^{15}O$) (Lee et al. 1999; Magadán-Méndez et al. 2010). In this last paper, the ICA projections were used to build regional masks using a fixed threshold on the independent component projection gray level.

While this method works on simple images just like the one previously shown, there are some caveats that have prevented its widespread adoption in this field: it is very sensitive to the number of independent components (a parameter that has to be set by the user) and is quite expensive computationally, especially in those cases that contain many different independent TACs (different organs or tissues); also, in those cases the final results are not as good as the ones obtained for simpler cases (Figure 1.17).

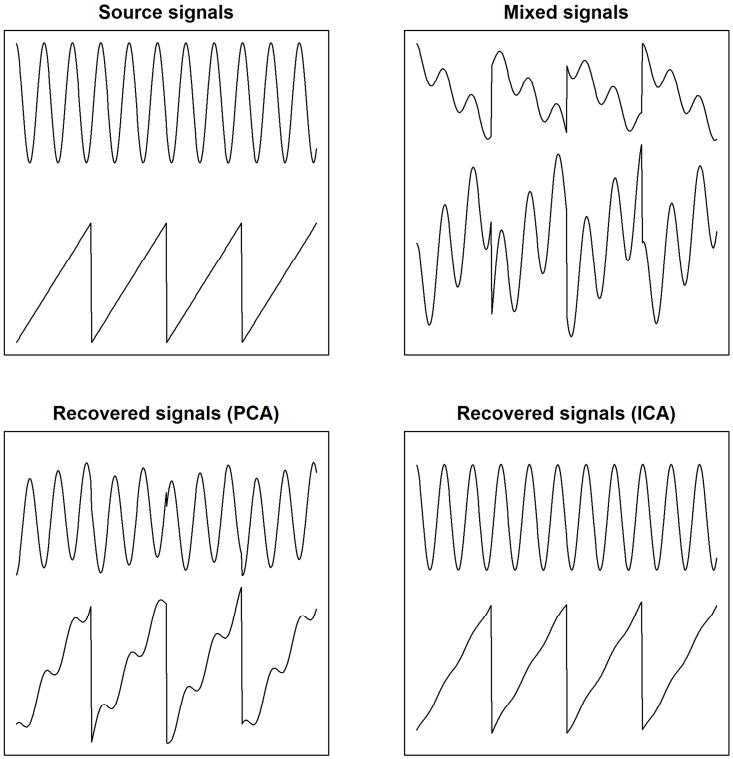

Figure 1.16: differences between how PCA and ICA extract different signals. While the principal components do not accomplish this task, the signals recovered by ICA resemble much more closely the original ones, presenting just minor distortions.

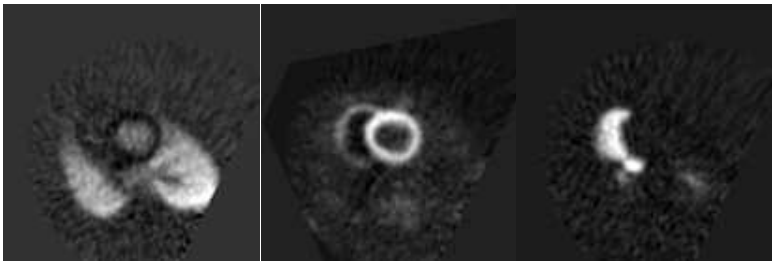

Figure 1.17: left ventricle (and lungs), myocardium and right ventricle regions extracted using ICA. A total of 7 independent components had to be extracted, with the rest of them showing only noise.

1.3.5 SCA

Similar component analysis (SCA), along with the next one (LMA), has been developed explicitly for the problem of functional segmentation of dynamic imaging sequences. As stated in the title of the publication that presented it (Brankov et al. 2003), it can be used to segment dynamic PET or fMRI (functional magnetic resonance) images.

In this work, the cosine between two given TACs is taken as the similarity metric used to test whether a given voxel should belong to a cluster or another. It uses a predefined number of classes, as k-means or ICA do, and then groups all the voxels in the image in one class or another using an iterative approach. The original paper demonstrated the feasibility of this method using phantoms, but the applications on real studies have been made generally in studies comparing different methods, as shown on the following section. In those comparisons it does not yield good results and is always dropped in favor of LMA.

As there are no available source code or public implementations of this algorithm, no images can be shown.

1.3.6 LMA

Local Means Analysis (Maroy et al. 2010; Maroy et al. 2008; Zanotti-Fregonara et al. 2009) is, to the extent of our knowledge, the latest published method that aims at solving the automatic functional segmentation problem. It is the method implemented PMOD from version 3.5 and, unlike SCA, we had the chance of trying it in our own images for comparison purposes.

This method, detailed in (Maroy et al. 2008), locates the image regions that are surrounded by voxels with similar dynamics and creates a map of local minima by computing the weighted distance between an individual voxel TAC and those of a neighborhood defined by a structuring element of a certain size. The weights are the length of each frame, so later frames, that are usually longer, carry more weight in this computation.

Once the local minima map has been computed, each point within that map is joined with adjacent points using the shortest path of minimum energy. Once all the points have been joined with all the other minima locations, a hierarchical linkage algorithm is used to generate as many different classes (*segments* in the terminology of this algorithm) as defined by the user.

While published comparisons have shown that this method yields superior results when compared to SCA and k-means, in our tests the results have been mixed. Consider for instance the two segmentations shown in Figure 1.18. The swine study used in this section has been segmented with this method with 10 (left) and 20 segments (right). Both the myocardium and the right ventricle have been correctly extracted, but the left ventricle is heavily mixed with the background lung. The mathematical formulation of this method might cause it to join together regions that have very similar kinetics if there is no barrier between them, as in this case; the

left ventricle and the lung activities in this particular example are very highly correlated and there is a very gradual loss in amplitude from the center of the image. Our preliminary tests confirm this hypothesis. This algorithm might be quite useful when trying to find regions that are very distinct to their surroundings, but in cases like this one, a new approach is needed.

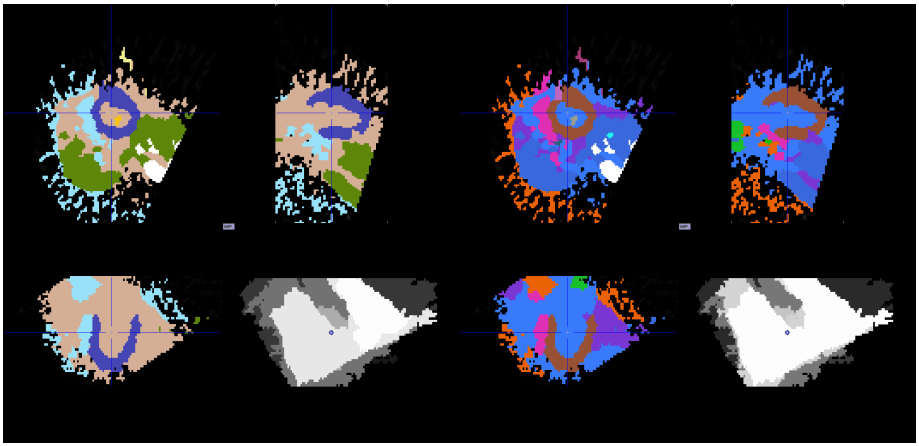

Figure 1.18: Local Means Analysis performed using PMOD 3.5 with 10 segments (left) and 20 segments (right).

1.4 Document outline

Chapter 1 introduces the theoretical background necessary to understand the mechanism of quantification of dynamic PET imaging, along with the most common problems and a brief review of the solutions proposed in the literature.

Chapter 2 lists the motivation and objectives of this work.

Initially, a supervised segmentation algorithm is presented and validated as a proof of concept. It is developed under the hypothesis that a study can be automatically segmented if the kinetics of similar studies are known and used as the training dataset. This is detailed in Chapter 3.

Chapter 4 describes the development of jClustering, an ImageJ plugin developed for the purpose of implementing new unsupervised segmentation (clustering) algorithms. Said plugin has been offered to the ImageJ community with an open license (GPL) and has been the main tool used for the further development of most of the algorithms presented in this thesis. Secondary software packages not directly related to the image segmentation problem are briefly detailed in chapter 5.

Chapter 6 explains the development of a new automatic segmentation algorithm based on a leader-follower approach and its validation using rodent studies. This chapter shows that the proposed algorithm is able to provide a segmentation that yields the same kinetic parameters as a manual delineation performed by an experienced user. Said algorithm was implemented under the tool detailed in the previous chapter and its source coded was published with an open license.

Finally, the conclusions of this Thesis are laid out in Chapter 7 and the publications derived from this PhD Thesis are listed in Chapter 8.

2 Motivation and objectives

2.1 Motivation

As stated in the previous section, the analysis of dynamic PET studies brought new opportunities as well as new challenges to the field of biomedical imaging processing. Correct study quantification involves obtaining accurate time-activity curves (TACs) for both the input function and the different tissues being measured. The quantification process involves fitting the tissue TAC using the arterial input function in order to obtain the kinetic parameters of the system, which provide absolute measurements about the metabolism, blood perfusion or other functional aspects of the organ or region of interest according to a certain model. This fitting process involves choosing a model that depends on the underlying biological processes under study.

Typically, the extraction of the relevant tissue TACs is done directly via manual segmentation over the reconstructed image. This is known to be a subjective, non-repeatable, time-consuming operation (Zheng et al. 2011; Soret et al. 2007). The arterial input function can be obtained this way when big vessels are present in the field of view (Zanotti-Fregonara et al. 2011), as is the case in cardiac studies, but even in this case there is some variability depending on the left ventricle region chosen to sample the activity (Vasquez et al. 2013). While in the case of small animal studies blood sampling is recommended, so the image-derived input function can be corrected with at least two blood samples, in many cases it is difficult and no blood sampling is done at all, leaving the researchers with the image-derived input function alone (O'Sullivan et al. 2010). These limitations may bias the outcome of the analysis depending on the person who segmented the original studies. This proves the need to approach this problem in an automatic, reproducible way.

A very fertile field in the literature deals with solving this problem using some kind of supervised or unsupervised classification (clustering) techniques. A brief review of these methods can be read on section 1.3. As most of these methods aim at extracting the TAC that best describes a certain tissue, this approach can be referred to as *functional segmentation* (Rousset et al. 1998; Parker 2005) to differentiate it from the classical, anatomical concept associated to this term. However, most of the published methods are hardly reproducible since access in very limited or non-existing (lack of source code or binary availability, for example) and do not benefit from an open development approach that mimics that of the scientific processes (Barnes 2010; Ince et al. 2012). Because of that, new methods are published in print but external research groups have limited access to them and in most cases cannot apply them to their own studies, for either comparison or validation purposes, without a re-implementation process that requires extensive knowledge and training that not always available. It is worth noticing that the quantification results can be influenced not only by the subjective variability of the segmented areas: some publications have compared the results of the quantification process

for dynamic PET studies across a range of software tools with conflicting conclusions (Dekemp et al. 2013; Tahari et al. 2013). While this problem is too broad to be addressed in this thesis alone, we believe open implementations of useful algorithms would help mitigating it.

2.2 Objectives

The main objective of this thesis project is to propose a series of automatic functional segmentation algorithms for dynamic nuclear imaging. All the software developed for this thesis has been implemented under an open source platform or alternatively, the code generated is offered in a public repository with a free software license in order to allow its redistribution and modification, and therefore maximizing its usefulness to third parties and enabling all the advantages of an open development model cited previously. Whenever possible, the novel developed algorithms and software packages have been validated against commonly used commercial alternatives. Helper tools developed as side projects of this thesis have also been openly published.

The following sections describe in more detail the different parts of this thesis.

2.2.1 Supervised segmentation algorithm

The first part of this thesis experiments with the possibility of using a supervised segmentation algorithm to extract both the input function and the tissue TACs and it has been applied to cardiac dynamic PET imaging. In this case, these different TACs can be learned from a set of studies and then applied to another in a way that allows the model to adapt to the variability of the target study. We present the validation of a proof of concept test using this method and its validation in three swine studies using $^{13}NH_3$ as tracer.

2.2.2 Clustering framework development

ImageJ (http://imagej.nih.gov/ij/), developed by the NIH, is a paradigmatic example of what can be accomplished by an open source program (in the public domain in this particular case) with a huge community of users and developers (Schneider et al. 2012). The success of this platform has allowed the creation of ImageJ distributions, like the Linux distributions, consisting on the basic package and a curated set of plugins; such is the case of Fiji (Schindelin et al. 2012).

One of the goals of this work is the development and public release of a framework for the development of dynamic imaging segmentation algorithms; specifically aimed at the implementation of clustering techniques (unsupervised machine learning algorithms). Said framework has been developed in Java and works as an ImageJ plugin. Its source code is publically accessible (https://github.com/HGGM-LIM/jclustering) under a free software license (GPL) to allow independent code reviews and modification by third parties. This platform has been used not only to implement the clustering algorithms presented in this thesis, but also some other algorithms that have been already extensively documented in the literature.

The elaboration of this thesis has required the development of other secondary software packages. They also have been published with an open license and are explained in detail in the appropriate chapter.

2.2.3 Leader-follower implementation

In (Duda et al. 2001) the *leader-follower* clustering method is presented as a variation over *k-means*; in this case, instead of a predefined, immutable number of clusters, the user can set a similarity threshold, according to a certain metric, that will determine the creation of new clusters. Therefore, the final number of clusters is unknown as the user inputs a value that will define the system tolerance; this value will determine how fragmented the final result will be. In this thesis, an open and improved implementation of this algorithm is presented. This algorithm has been validated using mice studies using several ^{68}Ga-DOTA-labeled somatostatin analogues as tracers.

3 Development of a clustering algorithm based on *a priori* models

(This text has been published as J. M. Mateos-Pérez, M. Desco, M. W. Dae, C. García-Villalba, L. Cussó, and J. J. Vaquero, "Automatic TAC extraction from dynamic cardiac PET imaging using iterative correlation from a population template," Comput. Methods Programs Biomed, vol. 111, no. 2, pp. 308–314, May 2013.)

3.1 Introduction

Quantitative kinetic analysis of dynamic cardiac PET data provides unique information that can improve discrimination between different states of myocardial tissue (Croteau et al. 2010; Joonyoung Kim et al. 2006). Conventional estimation of kinetic parameters based on compartmental models requires an accurate assessment of arterial blood input function. An image-derived input function removes the need for invasive blood sampling (Croteau et al. 2010; Weinberg et al. 1988; de Geus-Oei et al. 2006). One commonly used method involves manually defining a region of interest (ROI) (Croteau et al. 2010; Mourik et al. 2009; Tantawy & Peterson 2010; van der Weerdt et al. 2001). However, this can be a slow and challenging process, especially in noisy image series, where considerable care is needed to manually select the appropriate areas. Furthermore, the manual ROI segmentation process is operator-dependent and has low reproducibility (Wong et al. 2002). Therefore, a simple but reliable procedure to automatically extract the time-activity curve (TAC) would be advantageous, and several automatic or semi-automatic techniques have been proposed to address this issue. If these tools are to be applied in clinical practice, they should be user-friendly and provide consistent and reliable results.

Factor analysis of dynamic structures has removed the need for manual segmentation (Barber 1980; Di Paola et al. 1982; Wu et al. 1995). Although this approach is used extensively for semi-automatic TAC extraction, its main drawback is the non-uniqueness of the solution, which in practice is observed as spatial overlap between factor images from different regions (Joonyoung Kim et al. 2006). Several modifications to the original algorithm have been proposed to correct this problem (El Fakhri et al. 2005; Sitek et al. 2002) without using *a priori* information, mainly by imposing additional restrictions on those factor coefficients considered valid by the algorithm and thus penalizing overlap between regions. However, these modifications minimize but do not completely eliminate spatial overlap.

Other semi-automatic methods, such as covariance images calculated from an initial manual ROI, have been published (Boudraa et al. 1999), although they require manual intervention from the user.

Several proposed solutions involve clustering techniques (Zheng et al. 2011; Liptrot et al. 2004; Wong et al. 2002; Zaidi et al. 2002; Brankov et al. 2003; Zanotti-Fregonara et al. 2009; Maroy et al. 2008). For algorithms such as the classic *k-means* (Duda et al. 2001), it is important to know the number of clusters *a priori* to obtain an optimum result (Liptrot et al. 2004; Wong et al. 2002); however, this information is often unknown and it is not easy to compare results obtained with different values of *k* (Liptrot et al. 2004). Furthermore, *k-means* uses a random initialization process that may cause it to fall into a local minimum.

Since the dynamics of the tracer used are often well known, the solution to this problem could be simplified in order to extract the TACs using a previous kinetic model and a similarity metric. Prior modeling of the approximate solution has successfully applied in other applications (Hapdey et al. 2011).

We present proof of concept for an iterative clustering method that makes it possible to automatically obtain the image-derived blood input function and myocardial TACs from dynamic cardiac PET studies. We apply *a priori* models of tracer kinetic behavior in different regions or tissues obtained from a population sample and not from the study being segmented; this approach resembles *k-means* but requires considerable *a priori* knowledge of the problem. No manual intervention from the operator is necessary. In addition, the technique is fast and provides robust results based on the original data (which are therefore physiologically interpretable).

3.2 Materials and methods

PET studies using ^{13}N-ammonia (740 MBq) in healthy pigs were obtained at rest and under stress conditions. Images were acquired using a matrix size of 128 x 128 x 47 pixels, with a voxel size of 2.34 x 2.34 x 3.27 mm. Twenty-five dynamic frames were acquired over a total of 900 seconds (18 x 5-s frames, 2 x 15-s frames, 3 x 60-s frames, and 2 x 300-s frames). Tracer was injected as a bolus using an automatic device. All the studies were acquired using a Discovery STE scanner (General Electric Healthcare, Connecticut, USA) in 2D mode and reconstructed using a filtered back-projection algorithm at 2 mm/pixel with a 4.8-mm cutoff and no post-filtering or scatter correction with convolution subtraction. Images were masked to include only the relevant tissues.

The different regions (left ventricle, right ventricle and myocardium) were manually segmented and their mean TACs were obtained. TAC templates corresponding to these three different volumes of interest were generated using function fitting with nonlinear least-squares. Three TAC templates were generated, one for each pair of studies, in order to use a leave-one-out approach in the validation stage. The right and left ventricle TACs are defined by a gamma function according to the equation

$$f(t) = Kt^{\alpha} e^{-(t/\beta)} \tag{3.1}$$

The myocardium curve was modeled using an exponential plus a constant factor that corrects for late time slope, as follows:

$$f(t) = K(1 - e^{-t/\alpha}) + \beta t \tag{3.2}$$

Exact values of K, α, and β in these equations are fitted using as templates the curves extracted from the original studies. As these are the first models in the iterative process, their initial formulation does not necessarily describe the final result and it is indeed just an approximation. Furthermore, a gamma function fit does not provide as good a result as triple exponential or other similar functions; nevertheless, the purpose of the initial curves is to have a generic model of tracer behavior that is similar in shape to as many studies as possible. An example of these initial templates can be seen in Figure 3.1, along with the manually-derived curves.

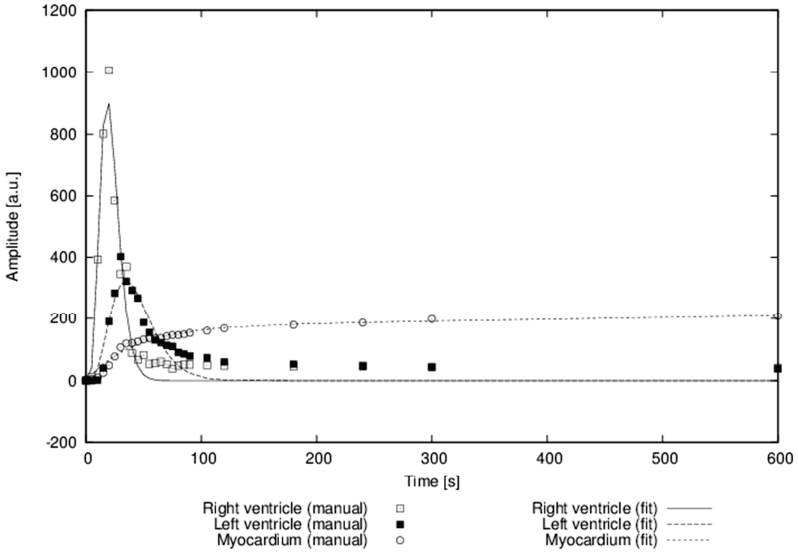

Figure 3.1: sampled image data and fitted functions using the approach described above.

The method proposed iteratively updates the TACs corresponding to the three regions, starting with the previously defined templates. The resulting curves are not fitted after each iteration; instead, the average TAC for the region is used. In each iteration, the method calculates three correlation images, one for each region (left ventricle, right ventricle, and myocardium). The value of each new voxel in these images is the result of computing the correlation for the TAC

of that particular voxel with the corresponding template. The Pearson correlation is used for this calculation as follows:

$$\rho_{X,Y} = \frac{\operatorname{cov}(X,Y)}{\sigma_X \sigma_Y} = \frac{E[(X-\mu_X)(Y-\mu_Y)]}{\sigma_X \sigma_Y} \tag{3.3}$$

with X and Y being any two TACs, and μ and σ their mean value and standard deviation, respectively. In our case, X will be the TAC from a given voxel and Y the TAC from the template.

Each iteration comprises three steps:

1. The correlation between the TAC measured for each smoothed voxel (3 kernel points, {0.25, 0.50, 0.25}) and the templates are computed. To avoid noisy TACs, the corresponding TAC maximum value must be positive and greater than the absolute value of the TAC minimum (which can be negative due to noise), otherwise the TAC is skipped. For those voxels that comply with these conditions, the largest of the three correlation values is assigned to the corresponding correlation image (left ventricle, right ventricle, or myocardium) if it is higher than a predefined correlation threshold and is set at zero in the other two images.
2. Each correlation image is filtered using a 3x3 median filter to eliminate isolated voxels. The remaining voxels are set at 0, thus resulting in a binary volume mask.
3. A new TAC for each region is calculated by averaging the TACs of those voxels determined by the masks, and this new TAC is used as the template for the next iteration.

The correlation thresholds used at each iteration are {0.2, 0.3, 0.4, 0.5, 0.6, 0.7, 0.8, 0.9, and 0.95} for a total of nine iterations. The rationale for these correlation scores is that the initial model comes from the fitted template and does not precisely represents the specific curves for the problem being solved; therefore, low correlation scores must be used to find the actual study curves that resemble those of the model. Once those curves have been found, spurious data are filtered out by steadily increasing the correlation score used.

After the final iteration, three volumes are obtained, one for each TAC (left ventricle, right ventricle, myocardium). Each volume contains the correlation values for every voxel. To define the final TACs, a two-step selection process is applied. First, in order to eliminate voxels with low correlation values from the final calculation, only those voxels whose correlation value is in the 70th percentile for each specific correlation image are kept. In the following step, the maximum TAC amplitude is computed for all the voxels corresponding to the left ventricle and right ventricle images obtained from the previous filtering. Finally, an average curve is computed from those voxels that have a TAC whose amplitude is above the 50th percentile. This step is only required for calculation of the ventricular cavity TACs and is needed to

remove low-amplitude voxels that smooth the final image-derived input function. The resulting images after this last step are also saved and used to visually check the regions from where the TAC was finally extracted. These images are offered only as a reference, as the actual results obtained by this algorithm are the TACs for each region.

The algorithm was developed in Java as a plug-in for the PMOD software package (PMOD Technologies Ltd., Zurich, Switzerland). All tests were carried out on an Intel Core 2 Quad CPU with 4 GB of RAM. ImageJ v1.42 (National Institutes of Health, Bethesda, Maryland, USA) and COLT v1.2.0 libraries (CERN – European Organization for Nuclear Research, Geneva, Switzerland) were used for image processing. This is the only algorithm presented in this paper that has not been developed with the help of *jClustering*. Initially, different segmentation algorithms were being implemented in the PMOD software, thanks to a special course for developers offered by PMOD Technologies Ltd. PMOD changed the internal API needed to develop plugins in new versions of the software and it was decided to move to a more open platform for automatic segmentation algorithms development. The code for the presented method, as a PMOD 3.1 plugin, can be obtained from https://github.com/HGGM-LIM/j.cmpb.2013.04.010.

To create a gold standard, all the studies were manually segmented by three specialists. Although the usual gold standard for these measurements is arterial sampling, such data were not available; therefore, the image-derived input functions were used as a surrogate measure (Croteau et al. 2010; Weinberg et al. 1988; de Geus-Oei et al. 2006). Furthermore, as this method was developed to extract the input function and tissue curves from image data, a comparison had to be made against the manually obtained TAC.

Due to the small sample size, cross-validation was carried out using a leave-one-out approach: templates were obtained with each pair of studies (study 1 and 2, study 2 and 3, study 1 and 3) and used to segment the remaining study. This is a cross-validation approach useful in studies where the number of cases is small, such as the present one. Mean TACs were generated for each region, the curves were fitted and used to segment the third study.

TACs obtained automatically and manually were compared using the normalized root-mean-square deviation (NRMSD):

$$NRMSD(\%) = \frac{\sqrt{\frac{\sum (TAC_{automatic}(t) - TAC_{manual}(t))^2}{n}}}{TAC_{\max} - TAC_{\min}} \times 100 \qquad (3.4)$$

where $TAC_{automatic}$ is the TAC obtained by the algorithm, TAC_{manual} is the average TAC for all the manual segmentations for that particular region, n is the total time points acquired, and TAC_{max} and TAC_{min} are the maximum and minimum values for both TACs.

The Pearson correlation coefficient between manual and automatic results was also computed. To perform a visual evaluation of the final segmentation, static images were created by adding the last five frames of the dynamic images.

Kinetic parameters (K_1 [ml/min/g] and k_2 [min^{-1}]) and myocardium blood fraction (v_{LV}, dimensionless) were computed using a 1-compartment model (DeGrado et al. 1996) implemented in PMOD's kinetic analysis module. All the kinetic parameters are shown as a pair consisting of a value and its standard error. This standard error is yielded by PMOD's iterative fitting process and is a measurement of the correctness of the kinetic parameter.

3.3 Results

The cross-validation process was completed successfully using a leave-one-out approach, and all the studies were segmented employing less than half minute computing time (17.86 ± 2.28 s; mean ± standard deviation). The TACs obtained automatically very closely resembled those obtained via manual segmentation, both in shape and in amplitude ($r \geq 0.97$ for all regions, Table 3.1).

Study	Left ventricle		Right ventricle		Myocardium	
	NRMSD (%)	r	NRMSD (%)	r	NRMSD (%)	r
#1	2.56 %	0.99	4.95 %	0.99	8.31 %	0.97
#2	6.38 %	0.99	5.84 %	0.99	6.35 %	0.99
#3	3.10 %	0.99	6.95 %	0.98	12.82 %	0.97

Table 3.1: final results (error and correlation score) of the comparison between automatic segmentation and an average manual segmentation curve.

An example of the resulting visual segmentation can be seen in Figure 3.2. It is important to note that visual segmentation is not the main outcome of this algorithm and is produced only for verification purposes. The TACs obtained for this segmentation are shown in Figure 3.3.

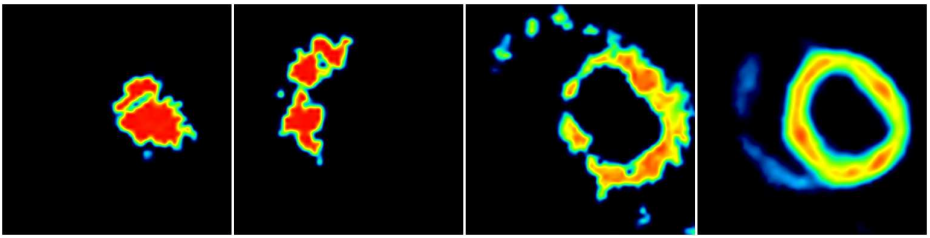

Figure 3.2: visual results of the segmentation process. From left to right, the different images are left ventricle, right ventricle, myocardium and a reference image obtained from summing the last frames of the study so the myocardium is clearly visible.

It can be clearly seen in Figure 3.3 that the right ventricle TAC obtained by the clustering method here presented is way below the mean activity obtained by the manual operators. That is due to the presence of an abnormally high manual segmentation that yielded 2000 Bq/ml maximum peak, while the other two yielded values of 1000 Bq/ml that are much closer to the peak value obtained by the automatic segmentation method.

The results of the kinetic analysis show that both the manually and automatically obtained curves yield similar results for myocardial blood flow (K_1), with the automatic TACs offering the smallest errors in the iterative process in almost all cases and the smallest spillover value from left ventricle into the myocardium (Table 3.2).

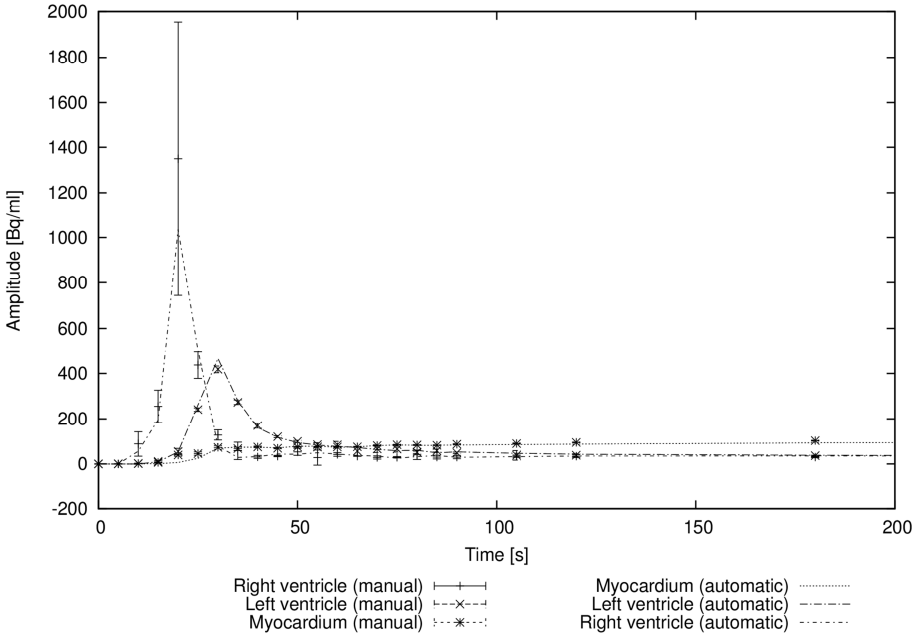

Figure 3.3: manual segmentation results (with error bars) and automatic segmentation activity curves (lines).

Study	K_1	Error	k_2	Error	v_{LV}	Error
#1, op 1	0.622057	5.49	0.118421	45.41	0.115477	14.07
#1, op 2	0.628333	3.66	0.106127	33.58	0.140943	7.57
#1, op3	0.651833	6.37	0.051074	116.43	0.127073	15.56
#1, auto	0.656951	2.17	0.2163	10.81	0.08639	7.06
#2, op1	1.094091	2.75	0.199012	15.48	0.164741	9.61
#2, op2	0.961911	2.44	0.141246	18.2	0.158114	8.06
#2, op3	1.17784	3.76	0.149479	27.28	0.167962	14.15
#2, auto	0.918549	1.88	0.206826	10.02	0.120561	7.17
#3, op1	0.489181	6.0	0.100358	56.61	0.15453	9.05
#3, op2	0.480133	3.04	0.101073	28.67	0.136645	5.17
#3, op3	0.46374	6.17	0.05567	101.18	0.149009	9.26
#3, auto	0.477204	2.45	0.250987	10.66	0.087988	5.81

Table 3.2: Kinetic analysis parameters. K_1 and k_2 are in ml/g/min. The Error parameter represents the coefficients of variation for that parameter after kinetic analysis modeling, in percentage.

3.4 Discussion and conclusion

The method proposed enabled us to successfully extract TACs for left and right ventricles and myocardium in all the studies after the leave-one-out cross-validation. The TACs extracted were then used as input in a kinetic analysis module, and the results show excellent agreement with those of the manually obtained TACs.

This method has several major differences with the classic *k-means* algorithm. First, the initial TACs are not obtained by selecting random voxels on the image, but are instead generated from a population sample, given that the kinetics of the tracer are known. Consequently, the results for the algorithm presented are deterministic, that is, they are always the same when applied to the same study, whereas *k-means* may fall into local minima (Liptrot et al. 2004). In addition, there is no need to find the optimal value of regions to be segmented (Wong et al. 2002; Zanotti-Fregonara et al. 2009), as the final result will yield as many TACs as templates used. Although only three templates were used in the present study, the algorithm could be used in principle with any number of regions.

No overlap was observed between the different regions; this is an improvement over factor analysis, in which overlap can be minimized in the factor images, but not completely removed (El Fakhri et al. 2005; Joonyoung Kim et al. 2006). Note that we are referring to image overlapping (that is, a voxel that simultaneously belongs to more than one region); spill-over and partial volume effects may still be present.

Despite the small sample size, the models accomplished their task and were used to locate similar curves inside the actual study. These curves were then refined; given that the correlation

score is increased every time, the number of pixels that is allowed inside each region diminishes with each iteration. In the graphical segmentations, the holes visible in some regions (e.g., right ventricle in Figure 3.2) are a consequence of the high correlation scores used in the last iterations of the algorithm. If the shape of a given TAC does not correlate highly with the one being used as the tissue TAC, that voxel will be skipped. As the objective of the segmentation process is to extract accurate TACs to be used as input in kinetic analysis procedures, imperfections in the visual result (which serves merely as a guide to the operator) are not relevant.

Use of a sample population as the training set for the initial templates is problematic. On the one hand, in order to automate this step in a clinical environment, a library with standard models can be defined for the most commonly used tracers. On the other hand, given that the algorithm needs *a priori* information, pathological tissue might not be correctly segmented if its kinetics is too different from that used to build the models. This may also be the case when the template has been generated using a different injection type. These problems could be solved by generating templates for different pathologies and injection types, although further testing should be carried out in this regard. Furthermore, failure to perform segmentation correctly may signal pathology when a healthy model has been used. In any case, pathology is less of an issue in the case of input function extraction, as its activity should be less influenced by cardiac pathology than surrounding tissues and is, in general, more robust than the myocardium TAC, as reflected by methods such as population-based input functions (Zanotti-Fregonara et al. 2012); this method would therefore provide a good input function extracted from the image data.

4 jClustering: ImageJ clustering framework

(This text has been published as J. M. Mateos-Pérez, C. García-Villalba, J. Pascau, M. Desco, and J. J. Vaquero, "jClustering, an Open Framework for the Development of 4D Clustering Algorithms," PLoS One, vol. 8, no. 8, p. e70797, Aug. 2013.)

4.1 Introduction

Dynamic nuclear imaging studies have become a common diagnostic technique in medicine, as they provide quantitative and functional information on several tissues thanks to the use of radiolabeled tracers with different *in vivo* behaviors (Krivokapich et al. 1989; Croteau et al. 2010; Sundaram & Freedman 2004; Lortie et al. 2007; Flotats et al. 2012; Valenta & Schindler 2012). In order to obtain accurate kinetic parameters for compartmental models (Gunn et al. 2002), it is first necessary to generate precise time-activity curves (TACs) both for the tissues being studied and for input functions, such as the TACs of the myocardium and ventricles in the case of a cardiac study. These curves can be obtained directly from the image by manually drawing regions of interest (ROIs), although this is a slow, time-consuming, subjective process (Prieto et al. 2012; Wong et al. 2002; Razifar et al. 2009). In order to avoid these problems, many automatic or semiautomatic segmentation algorithms have been developed over the years. These algorithms group together regions of the image with similar kinetics in order to obtain mean activity curves and thus improve the signal-to-noise ratio. Examples of these algorithms include principal component analysis (PCA) (Pedersen et al. 1994), *k-means* clustering (Wong et al. 2002), factor analysis (Klein et al. 2008; El Fakhri et al. 2005; Sitek et al. 2002), hierarchical clustering (Guo et al. 2003; Liptrot et al. 2004), leader-follower clustering (Mateos-Pérez et al. 2011), segmentation based on TAC similarity metrics (Brankov et al. 2003), multiphase level set methods (Cheng-Liao & Qi 2010) and independent component analysis (ICA) (Magadán-Méndez et al. 2010; Lee et al. 2012).

One of the problems affecting many algorithms is unavailability of source code (Ince et al. 2012), not even in binary package form. Consequently, interested researchers, who may not have a technical background, are forced to re-implement the algorithms in order to use them or perform comparisons with their own methods. Algorithm reimplementation requires programming knowledge and is open to errors.

As a preliminary test, the source code for 11 previously published articles on new dynamic PET segmentation algorithms (all published after 2002) was requested by e-mail, and all responses were gathered over a one-month period. Four error messages were received, because the e-mail address was no longer valid. One respondent stated that the algorithm was patented and therefore no source code could be provided, one claimed that the code was already obsolete, one reported that the code had been developed by another person and refused, and three e-mails

went unanswered or were answered once with no follow-up. Only one author sent the requested code.

This paper presents *jClustering*, an open source tool and framework developed to facilitate implementation of segmentation algorithms for dynamic molecular imaging, but that can be potentially used for any dynamic medical imaging modality, such as dynamic contrast-enhanced magnetic resonance studies. In order to accomplish this purpose, the tool was written in Java, a programming language that does not require any kind of use fee and has an internal structure that lets the developer or researcher concentrate on the specifics of the algorithm. Furthermore, it is published under GNU GPL, a free software license, to allow code reviews and modification by interested third parties.

4.2 Materials and methods

4.2.1 Programming languages and design considerations

As *jClustering* was designed to simplify the implementation of new segmentation algorithms in dynamic nuclear medicine studies, image handling (e.g., loading, saving, displaying) was separated as much as possible from segmentation. Therefore, it was decided that this tool would be developed as an ImageJ plugin (Schneider et al. 2012). ImageJ is an imaging processing platform developed by the National Institutes of Health (Bethesda, Maryland, USA) with a very active community of users and developers and many different plugins and macros developed by this community (Schindelin et al. 2012). It provides an open and stable API that performs the background tasks and allows easy and reliable 4D (3D plus time) image manipulation.

The tool presented here was developed using Java (Oracle Corporation, Santa Clara, California, USA), as ImageJ is written in this programming language. Developing with Java is free and therefore fits with the objectives of the project.

4.2.2 Processing workflow overview

The process of generating cluster images by temporal similarity involves the analysis of all the TACs in order to group them into different classes, each with a mean activity curve, according to a specific algorithm. These classes are then said to define different regions in the subject according to variations in their kinetics.

The workflow implemented was kept as simple as possible and is depicted in Figure 4.1. In short, each individual voxel TAC is passed to the *ClusteringTechnique* module, which can re-use a *ClusteringMetric* if the metric of a particular algorithm has already been used. This *ClusteringTechnique* module groups together objects of the class *Voxel* (which contains TAC data and spatial information) using the *Cluster* class and adds all the formed *Cluster* objects to a native *ArrayList* object. Then, the final *ArrayList* object is automatically converted to an *ImagePlus* object for cluster visualization, since it is a native ImageJ image object. In order to

present the clusters comprehensively, a pseudo-dynamic image containing $n + 1$ frames is used, with n being the total number of clusters formed. The n^{th} frame contains the visual information for the n^{th} cluster, and the last frame contains a simultaneous composition of all the clusters for better spatial reference. This simplified workflow will be expanded in the following section as the relevant classes are discussed.

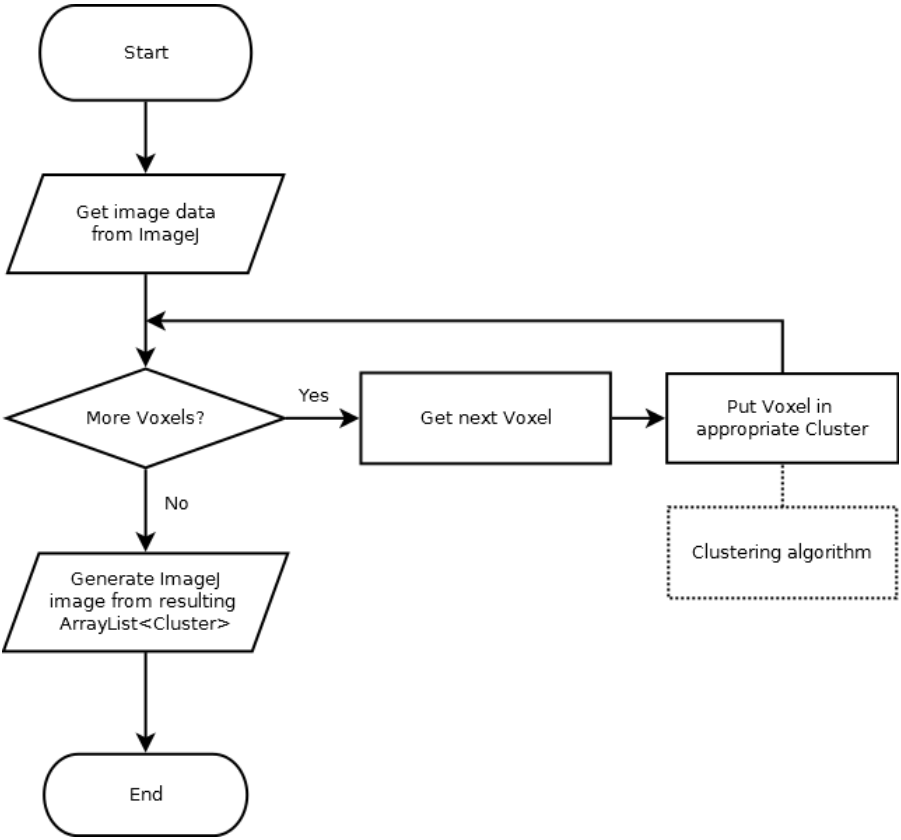

Figure 4.1: Flow diagram of the basic steps necessary to perform a clustering operation. In iterative algorithms, several loops of the voxel assignation stage can be performed until convergence is reached.

4.2.3 Relevant implemented classes and methods

4.2.3.1 ImagePlusHyp

The clustering algorithm reads the 3D image temporal sequence as a set of individual TACs, each of which corresponds to a single voxel.

ImageJ stores 4D images, called HyperStacks, as 3D images in which the slice number is proportional to the number of slices and frames combined (e.g., a HyperStack with 20 slices and 20 frames will contain 400 slices); therefore, obtaining the temporal TAC values for a given voxel involves inspecting the slices in the correct order. To simplify this procedure, a wrapping class (*ImagePlusHyp*) was created. This class serves as a proxy interface for the native ImageJ classes *ImagePlus* and *ImageStack*, thus enabling them to be handled efficiently for this TAC extraction task; the developer only needs to provide the coordinates for the desired voxel using the *getTac(int x, int y, int slice)* method, and the corresponding TAC will be returned. Furthermore, this class provides an *ImagePlusHypIterator* object that implements an *Iterator* interface which returns, one by one, all the voxels within the image for convenient use inside loops; the advantage of using the iterator instead of calling the *getTac(int x, int y, int slice)* method directly is that the iterator checks if the voxel has been masked (that is, all the values of the corresponding TAC are 0) and does not return it. This support for a prior masking step allows the user to reduce the complexity of the clustering problem being solved by eliminating those voxels that are known to belong to the background, for instance. The voxel information is contained in a *Voxel* class that stores a reference to the TAC data as a *double[]* and the *x*, *y*, and *slice* coordinates (the *slice* coordinate can be thought of as a 1-based *z* coordinate, or $z + 1$), in case the spatial information is needed.

4.2.3.2 Cluster

The *Cluster* class represents a grouping of voxels defined by a mean TAC known as a *centroid*. A *Cluster* may work in two different ways: either an invariant centroid is generates upon creation of the cluster and serves as a fixed reference or it is modified as new voxels are added to the cluster. This behavior is controlled by the constructor used: *Cluster()*, *Cluster(double [] centroid, int x, int y, int slice)*, and *Centroid(Voxel v)* create a *Cluster* object that will modify the centroid with each new addition. Such an approach is valid, given that a *Cluster* that is created from a single voxel is not using the centroid from a previous *Cluster* and may therefore be subject to change. *Cluster(double [] centroid)*, on the other hand, creates a *Cluster* with an immutable reference centroid and computes a mean cluster TAC with each addition.

4.2.3.3 ClusteringTechnique

ClusteringTechnique is an abstract class containing methods that must be implemented by extending classes in order to perform the actual clustering. It is also the main class, and often the only one that an external developer should extend when implementing a new clustering algorithm.

Internally, the tool creates an instance of the chosen extending class and initializes certain internal values so that the object is in a consistent state, including a reference to a *ClusteringMetric* (if needed), a reference to an initialized but empty *ArrayList<Cluster>* that will contain the *Cluster* objects generated, and a reference to the image data in the form of an *ImagePlusHyp*.

The only method that must be implemented is *process()*, which must fill in the *ArrayList<Cluster>* object with the appropriate *Cluster* objects. Should the algorithm require user input, the *makeConfig()* method, which returns a *JPanel*, must also be implemented, although user input is completely optional.

Although the *Cluster* objects will be automatically shown on screen with the correct formatting, the developer may also show additional images using the ImageJ native methods at this point, if necessary. Also, a *String[]* object can be filled with additional information; if present, this information will be saved along with the TAC data in the same directory.

4.2.3.4 ClusteringMetric

In order to promote re-use of code, the *ClusteringMetric* abstract class was implemented. Some clustering algorithms, such as k-means, group voxels together according to a specific distance, which may be the Euclidean distance, the correlation or covariance scores between two given TACs, or more elaborate metrics such as the Mahalanobis distance. Algorithms such as k-means can benefit from sharing code in the form of a *ClusteringMetric*, which computes the distance between two given TACs and only needs to be implemented once.

The *ClusteringMetric* abstract class has only one method that must be extended, namely, *distance(double [] a, double [] b)*, which computes the distance between these two arrays. As in the previous class, if a configuration dialog is needed, the developer can implement the *makeConfig()* method.

As some metrics (e.g., the Mahalanobis distance) may need to process initial data (in this case, the covariance matrix for the image), an *init()* method is provided; for this purpose, the *ClusteringMetric* objects also contain a reference to enable access to all the image data. This method is called once by the *ClusteringTechnique* before any call to the *distance()* method and can be used to initialize the necessary variables.

Figure 4.2 shows a diagram of the relationships between these classes.

4.2.4 Algorithms implemented

In order to provide an example of the capabilities of the framework, several clustering algorithms and metrics were implemented, as follows: *k-means* (Duda et al. 2001), *k-means++* (Arthur & Vassilvitskii 2007), *leader-follower* (Mateos-Pérez et al. 2011), PCA (Pedersen et al. 1994), singular value decomposition (SVD) (Duda et al. 2001) and ICA (Magadán-Méndez et al. 2010). The metrics implemented, which can currently be used by the *k-means* algorithm, are the Pearson correlation score, p-norm (p = 1 for Manhattan distance and p = 2 for Euclidean distance), and Mahalanobis distance.

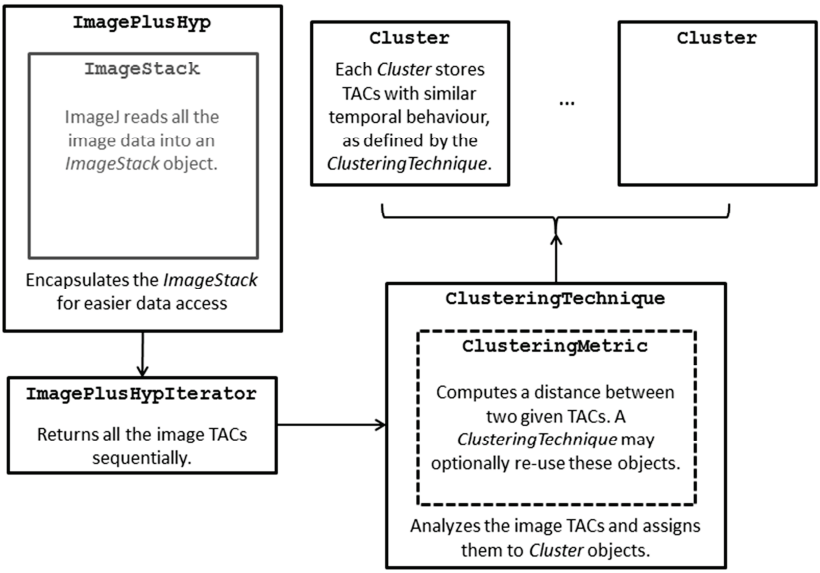

Figure 4.2: diagram of the main classes. Only the most relevant classes implemented are included in the diagram. Helper classes (eg, for GUI building or mathematical libraries) are not shown.

The Pearson correlation distance is computed as

$$\rho = \frac{1}{(n-1)\cdot\sigma_a\cdot\sigma_b}\sum_t (a(t)-\bar{a})\cdot(b(t)-\bar{b}) \tag{4.1}$$

where *a(t)* and *b(t)* are the two TACs, $\bar{a}$ and $\bar{b}$ are the mean values for those TACs, σ_a and σ_b are the standard deviations and *n* is the length of the sequence. In order to turn the correlation into a distance, the method returns $distance = 1-\rho$.

The generalized p-norm metric is defined as

$$distance = \left(\sum_t \left|a(t)-b(t)\right|^p\right)^{\frac{1}{p}} \tag{4.2}$$

This metric has a configuration panel that allows the user to set the value for the *p* parameter (defaults to 2.0, Euclidean distance).

The Mahalanobis distance is defined as

$$distance = \sqrt{(a-b)^T S^{-1} (a-b)} \tag{4.3}$$

where S is the covariance matrix for the image; to speed up computation, this matrix is computed just once, using the *init()* method.

Finally, the root-mean-squared deviation (RMSD) is defined as

$$distance = \sqrt{\frac{\sum_t (a(t)-b(t))^2}{n}} \tag{4.4}$$

4.2.5 Graphical User Interface (GUI)

A simple GUI was built. It contains three separate tabs: the main configuration tab, the technique configuration tab, and the metric configuration tab (the last two tabs may be empty if no configuration is needed). The main configuration tab makes it possible to select a directory in which to store a text file. This text file stores the values of the TACs for every cluster so that they can be used as input in subsequent analyses. *jClustering* can store this text file in comma- or tab-separated values or in PMOD (PMOD Technologies Ltd., Zurich, Switzerland) format.

Currently, ImageJ does not extract the frame information (start and ending times) from the image metadata. This problem was solved by complementing the main interface with a selection button to provide a file containing the frame start and end times in a tab- or space-separated text file with two columns and as many rows as frames. The resulting temporal data, which are essential for kinetic analysis, are stored in the first two columns of the resulting text file that contains the different TACs and can then be entered into a kinetic analysis program such as PMOD.

4.2.6 Input image formats

One of the advantages of developing tools for *ImageJ* is that the package manages image I/O. *jClustering* is able to deal with any image format that *ImageJ* can open, provided the contents are a dynamic image, either 2D + time or 3D + time; upon opening a file, the image data is internally assigned to an *ImagePlus* object that is directly handled by *jClustering* classes. If the image is static, a warning is shown. The test images used in this paper are stored in either DICOM or Analyze format; in other tests, raw images have been converted to an *ImageJ* HyperStack and processed.

4.2.7 Class autodetection

New *ClusteringTechnique* and *ClusteringMetric* child classes are automatically detected if they belong to their corresponding packages and are stored in the right directories (*jclustering/techniques* and *jclustering/metrics*, respectively) and the necessary GUI elements are updated accordingly. External developers are thus freed from the added burden of having to modify the core *jClustering* files to add their own classes.

4.2.8 Licensing

To ensure that third parties are able not only to extend but also to modify and adapt this tool, a free license is the best option. In this case, the source code is licensed using a GNU General Public License (GPL).

Even though development started privately, once a stable release could be provided, all the code was copied to a public git (http://git-scm.com/) repository (https://github.com/HGGM-LIM/jclustering) and all subsequent development was public.

4.2.9 User documentation

A user and developer manual have been published. They contain enough information to use this tool or to develop new plugins using its public API. They can be downloaded from https://github.com/HGGM-LIM/jclustering/blob/master/doc/user_manual.pdf?raw=true and https://github.com/HGGM-LIM/jclustering/blob/master/doc/developer_manual.pdf?raw=true, respectively.

4.2.10 Installation

jClustering installation is straightforward, considering it has been coded as a plugin for the ImageJ platform. Users need to download the latest jClustering_.jar file from the download site (https://github.com/HGGM-LIM/jclustering/releases) and copy it to their *plugins/* directory in their local ImageJ installation. Apache Commons Math and FastICA libraries are also needed; they must be copied in the *plugins/jars/* directory in their local ImageJ installation. A link to these libraries is provided in the main jClustering development page (https://github.com/HGGM-LIM/jclustering).

Once these files have been copied, jClustering can be run from the main ImageJ menu under *Plugins > Clustering*.

The source code is provided as a Maven repository, which allows developers to easily create their own projects and compile *jClustering* into a .jar file.

4.3 Results

Figure 4.3 shows a segmentation of a dynamic PET study using a *k-means++* algorithm (k = 10) with Euclidean distance as a metric (p-norm with p = 2). The image dimensions are 128 x 128 x 47, 25 frames, and the total time used in the segmentation was 20.15 seconds. Several principal components from a PCA of this image are shown in Figure 4.4; a total of 25 principal components were computed in 14.20 seconds. Figure 4.5 shows a simple segmentation of a dynamic human MRI study with gadolinium as a contrast agent using a grayscale LUT. The image dimensions are 128 x 128 x 28, 40 frames, and the total processing time is 10.47 seconds.

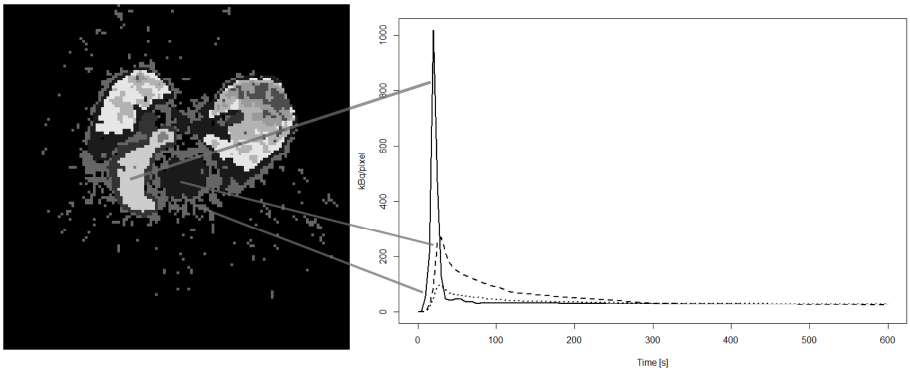

Figure 4.3: clustering results for a $^{13}NH_3$ pig study using a k-means++ algorithm (k = 10). The myocardium, the right ventricle, the left ventricle, and the lungs are clearly delineated. The activity curves for some relevant regions (right ventricle, left ventricle, and myocardium; right panel) are plotted from the text file stored by jClustering after segmentation.

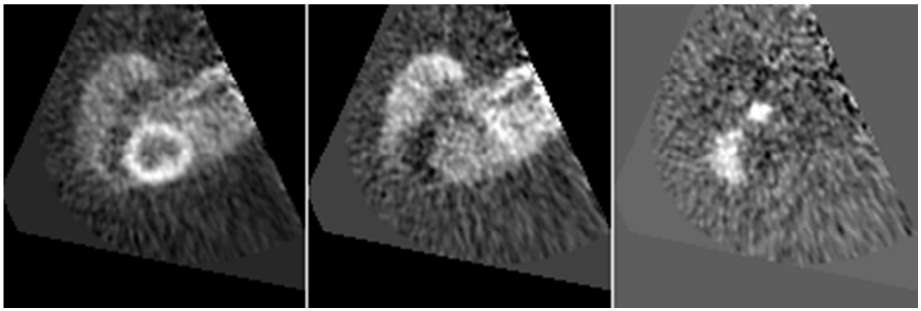

Figure 4.4: three principal components resulting from applying PCA to the same study as the one used to generate Figure 4.3. They have been chosen to represent the myocardium (left), blood pool (center) and right ventricle (right).

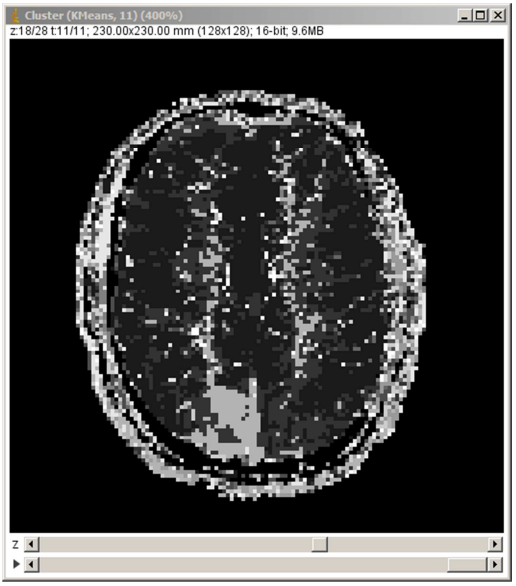

Figure 4.5: Clustering results for a dynamic MRI study using gadolinium as a contrast agent in a human subject. A lesion can be seen clearly at the bottom of the image. In this case, the full image screen is shown to highlight the ImageJ frame and the dynamic image controls that allow the user to switch between the different classes or, as in this case, a last frame containing all the classes, each with a different gray level.

4.4 Discussion

Although several papers have been published on automatic or semiautomatic dynamic imaging segmentation, very few include or even make available the source code of the algorithms developed. It can be difficult or even impossible to obtain the source code from the authors, as the contact address is no longer valid, the original code has been lost, or the author refuses to deliver it. Obviating the need to trace an author would leave the researcher free to focus on the solution to the problem and not on avoidable distractions. Occasionally, the source code can be obtained, only to discover that it has been implemented in a programming language that requires a fee for use. The development and publishing of an open platform that addresses this particular drawback makes sense not only from the point of view of offering a standard tool for free development, but also because it encourages code sharing and publication, which creates numerous advantages (Barnes 2010; Ince et al. 2012), including the possibility of receiving code reviews from third parties that can disclose previously undetected bugs.

Furthermore, publication of the source code for a new algorithm would help researchers to compare methods without having to re-implement each one using hard copy, which is a slow and error-prone process that could require further programming expertise. It would be better if

algorithms could be executed in a common segmentation platform such as the one presented here.

jClustering addresses these issues by providing a free and open clustering framework for effortless implementation of new clustering algorithms (see Appendix A for a simple example). As image-handling is delegated to ImageJ, new functionalities can be implemented using the remaining structure.

jClustering works in the Windows, Linux, and Macintosh operating systems. It does not use machine-dependent code or libraries and runs on the same platforms as ImageJ.

In this paper, *jClustering* is presented using dynamic studies in the context of nuclear medicine. However, Figure 5 (a successfully segmented dynamic perfusion brain study using magnetic resonance imaging) illustrates how this tool can be used with any kind of temporal image sequence.

jClustering is subject to a series of limitations. For instance, it cannot perform *fuzzy* clustering, in which every voxel is assigned a probability of belonging to a given cluster. All the segmentations performed with the current structure and class hierarchy associate a voxel with a region in a deterministic way, although it would be possible to implement the necessary changes to allow *fuzzy* clustering to work within this framework. This first approach allows some of the most common clustering algorithms, such as k-means, to be implemented. This drawback is in part mitigated with the possibility of generating additional information, both in image and text form, during the clustering operation (see Figure 5, for example).

Furthermore, *jClustering* cannot obtain the temporal information from the image metadata, which is a fundamental parameter for kinetic analysis. These data must be extracted from the image header, if present, by the user and stored in a text file.

jClustering works for ImageJ versions posterior to 1.46r, although it is not ready for the new ImageJ2 branch, which is expected to finish beta testing in December 2013. We decided to use the regular ImageJ distribution, which is currently the most widely used, has a stable application programming interface (API), and will be maintained for years to come.

The current version (1.2.2 at the time of writing) provides a stable API and already contains implementations of *k-means*, *k-means++*, *leader-follower*, ICA, PCA and SVD applied to image segmentation, although more methods should and will be added; hence the development of *jClustering*, a common platform for processing of clusters in dynamic medical imaging.

4.5 Conclusion

jClustering is an open framework for the implementation of dynamic imaging segmentation algorithms. It uses *ImageJ* capabilities to open, save, and display images, leaving the developer with the task of implementing new algorithms. Its source code has been made public under a free software license (GNU GPL) and is available, along with documentation and a link to binary releases, at https://github.com/HGGM-LIM/jclustering.

5 Secondary software packages

5.1 traceRkinetic: an open kinetic modeling library using R

(Part of this section was published in J. M. Mateos-Pérez, M. Desco, and J. J. Vaquero, "Tracer Kinetic Modeling with R for Batch Processing of Dynamic PET Studies", in XIII Mediterranean Conference on Medical and Biological Engineering and Computing 2013 SE - 75, 2014, vol. 41, pp. 301–304.)

During the initial steps of this thesis, the PMOD software package was used for kinetic modeling of dynamic PET studies. This software has been extensively used in the literature and can be considered a *gold standard* for kinetic analysis

However, for a large number of studies, the use of PMOD could be quite slow. Thought it has a "batch mode" that is intended to apply several operations to the same study, or to a set of studies, it does not allow to apply the same operation to a large number of files, as would be desirable, unless they have been previously preprocessed with PMOD itself, and this is because the batch mode does not work with raw (ASCII) TAC files.

As part of this thesis, an R library that performs kinetic modeling has been developed and validated in studies using different tracers. This library allows reading the input function, the tissue activity values and the time information (frame start and end times) from an ASCII file in different formats and returns the tissue kinetic parameters. The frame length can be used to weigh each point using a weighted non-linear least squares fit as suggested in (Lortie et al. 2007). The implementation used in this library delegates the actual fitting process to the *minpack.lm* package (Elzhov et al. 2012), which calls a Levenberg-Marquardt routine using the *MINPACK* library (http://www.netlib.org/minpack/). This was done in order to get an implementation as similar as possible to PMOD's, as this algorithm is its default method. The default initial values used in the fitting process are the same that PMOD uses, as are the upper and lower parameter limits for the rate parameters, though other values can be passed to the fitting function if needed.

As each frame has a different length, a linear interpolation was made to obtain frames of a length of one second that could be used in the convolution operation. Original data points are assigned to the end of their containing frame. Points outside the sampling range were linearly extrapolated.

The function plots the fitting results as PMOD does, so the user can verify the final fit quality. An example of a fitted study can be seen on Figure 5.1. The original data is shown alongside the

fitted values; the title shows the study that has been fitted so that several studies can be batch-processed and checked afterwards.

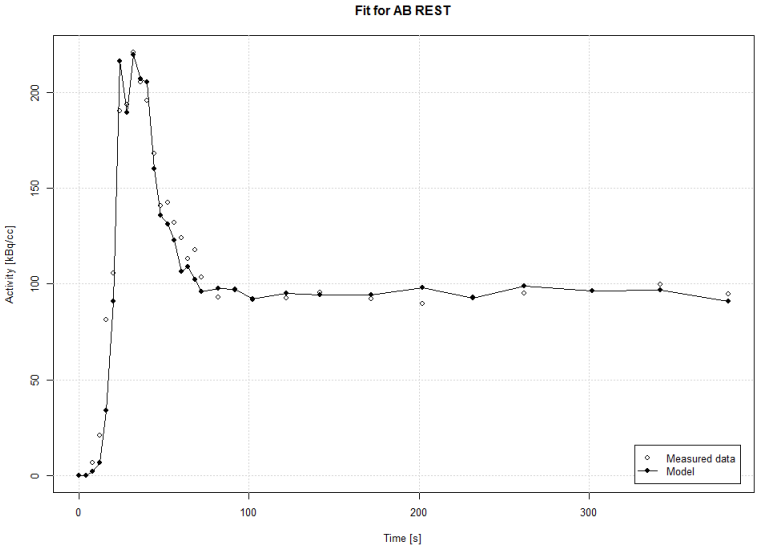

Figure 5.1: example of a ^{82}Rb fit with the R implementation.

In order to test whether this method yields the same results as PMOD 3.3 and therefore can be used as a substitute, 16 ^{82}Rb studies (eight rest, eight stress) were quantified using both programs and the values for K_1 and k_2 were compared for the one-tissue compartment model; also, ten mice studies using ^{68}Ga-DOTA-based tracers were used to validate the two-tissue compartment model. The fit was done using the same upper and lower parameter limits and the same initial estimates, as provided by the PMOD default values.

The results for this comparison can be seen in Figure 5.2, Figure 5.3 and Figure 5.4. The correlation between the kinetic parameters is good for both methods ($R^2 > 0.99$, $p < 0.001$ in all cases) and the Bland-Altman plots do not show any identifiable bias in the results. The differences observed are smaller than the standard error for each parameter.

The total time employed by the fitting function was 0.34 seconds for the 16 fits needed to perform the comparison for the one-tissue compartment model and 10.05 seconds for the ten subjects in the two-compartment model.

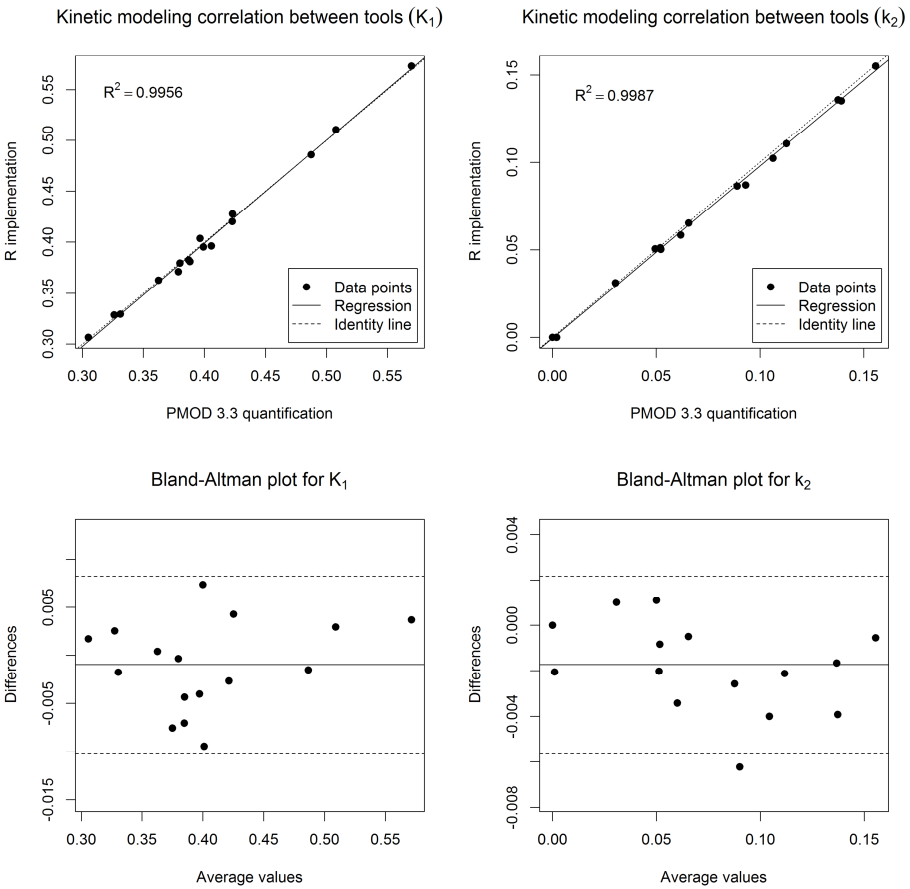

Figure 5.2: agreement between the K_1 and k_2 values for both the PMOD and the R implementation quantification. High correlation scores are obtained for both processing methods and the Bland-Altman plots permit to assess the high level of agreement between the two methods and it shows there is no bias in the results. Dashed lines in the Bland-Altman plots represent the 95% confidence intervals.

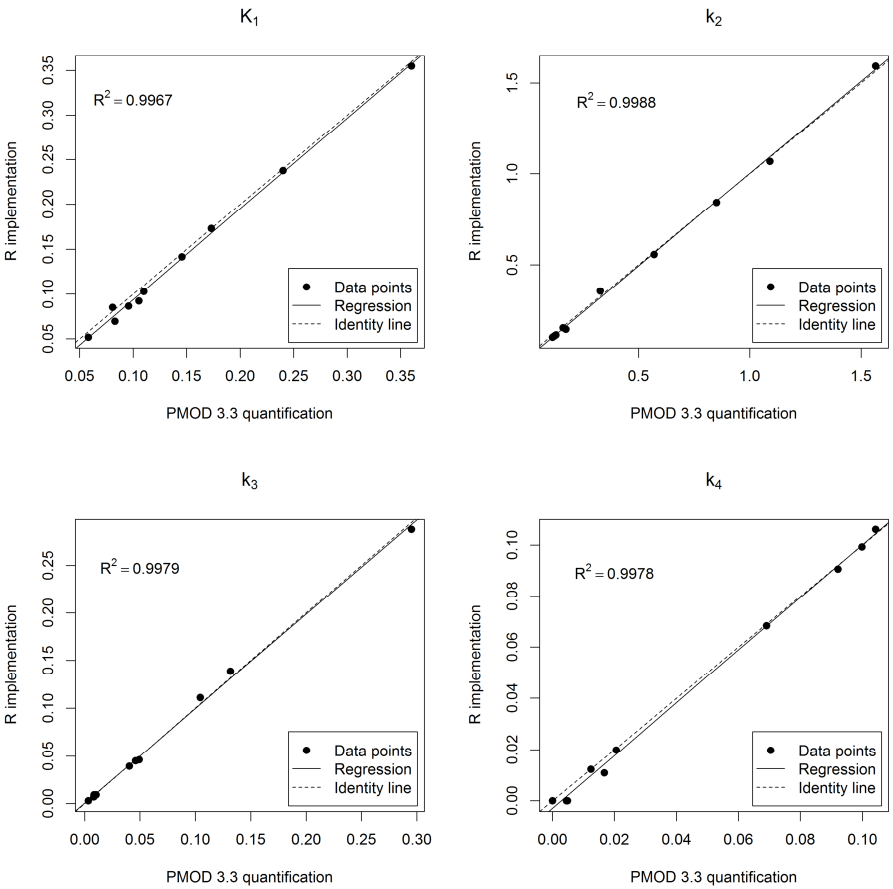

Figure 5.3: correlation between the different kinetic parameters obtained using R and PMOD 3.3.

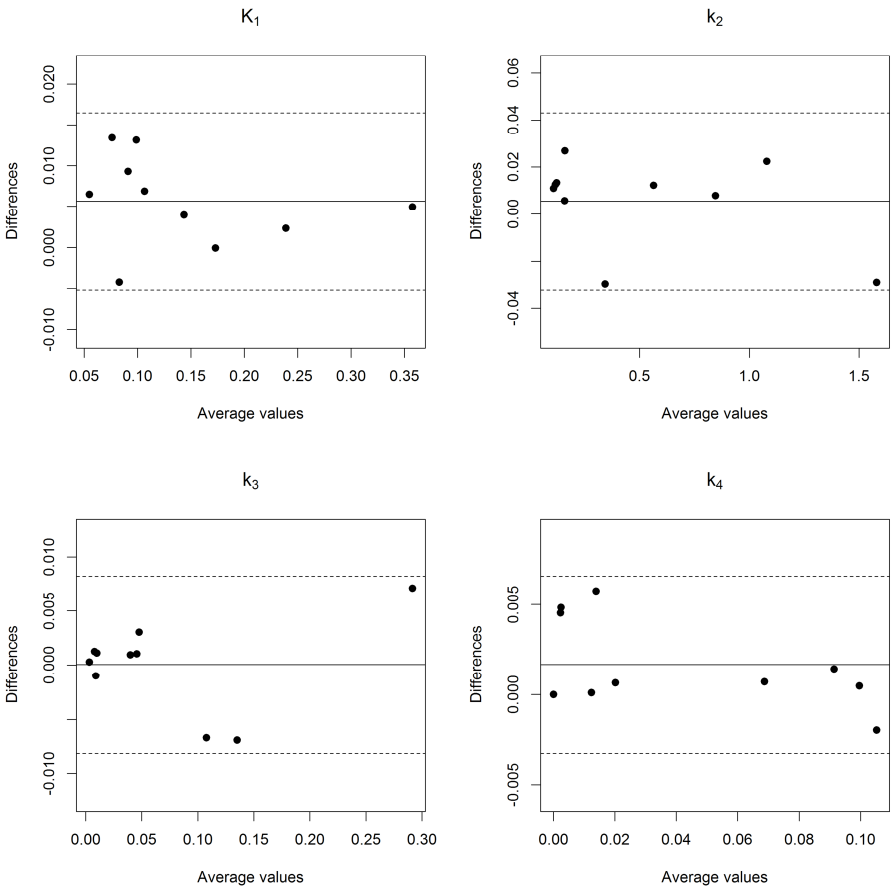

Figure 5.4: Bland-Altman plot of the kinetic parameters obtained using R and PMOD 3.3. Dashed lines represent the 95% confidence interval.

Also, the linear and multilinear methods detailed in section 1.2.2.3 have been implemented. Patlak and Logan methods are also implemented and have been compared with PMOD, yielded good agreement scores ($R^2 > 0.90$ for Patlak, $R^2 > 0.99$ for Logan). Compared to Logan, MA1 obtained a $R^2 > 0.98$, and MA2 $R^2 > 0.88$. Regarding the Patlak substitutes, MLAIR1 obtained $R^2 > 0.87$ and MLAIR2 $R^2 > 0.75$.

Therefore, it has been shown that for our purposes this library can be used as a replacement for PMOD since it is more flexible regarding the kind of input files it accepts and allows us to process several studies in a single batch.

The source code for this kinetic modeling library can be downloaded from https://github.com/HGGM-LIM/tracerkinetic/.

5.2 LIM Tools ImageJ plugin set

It is worth mentioning the development and publication of another ImageJ plugin set, named "LIM Tools", that implements several dynamic imaging functionalities not available under ImageJ but that were needed at the time this PhD thesis was being developed. This small toolbox does not need a whole chapter in this text but deserves a brief mention. At the time of this writing, this plugin set includes tools for:

- Averaging all or a subset of the frames in a given study.
- Graphical inspection of the TACs in a certain volume by moving the mouse pointer over the image.
- Storing dynamic data to disk in text format (for parametric map generation using traceRkinetic) and conversion from text files into dynamic images.
- Masking a dynamic image using a static mask, often the result of some kind of histogram masking over an average of the whole volume.
- Getting TACs from selected areas of the image.
- Jaccard and Dice indexes computation.

This toolset can be downloaded from https://github.com/HGGM-LIM/limtools.

6 *Leader-follower* implementation and validation

(This text has been submitted for publication as J. M. Mateos-Pérez, M. L Soto-Montenegro, S. Peña-Zalbidea, M. Desco and J. J. Vaquero, "Automatic functional segmentation of dynamic PET studies: a leader-follower-based algorithm open source implementation and validation".)

6.1 Introduction

Dynamic nuclear imaging analysis enables the quantification of the response of different biological tissues more precisely than a static acquisition in different types of studies, such as myocardial blood flow (Dekemp et al. 2013; Lortie et al. 2007) and glucose metabolism (Huisman et al. 2012). It also allows assessing lung inflammation in small animal studies (Pérez-Campaña et al. 2013) and specific biological receptor activity using specially developed tracers (Hostetler et al. 2012; Tsujikawa et al. 2013).

The quantification process for these studies involves obtaining the time-activity curves (TACs) for the relevant organs or tissues and the arterial blood, also known as the input function (IF). Continuous blood sampling by arterial catheterization is generally considered the gold-standard for IF estimation (Bentourkia et al. 1999), but this technique is invasive, causes patient discomfort and presents additional difficulties in experiments involving small animals (Schain et al. 2013; Pain et al. 2004; Meyer et al. 2006). It has been shown that the input function can be obtained directly from the image data in human studies under certain conditions, such as the presence of big blood pools in the field of view (Zanotti-Fregonara et al. 2011; Chen et al. 1998). In the case of small animal studies it is also possible to extract the image-derived input function from the heart or abdominal aorta and use just one or two blood samples to correct for partial volume and spill-over effects (Xiong et al. 2012).

All these image-derived IF (IDIF) methods involve the manual delineation of the relevant structures over the image, which is a user-dependent and time-consuming process (Wong et al. 2002; Slomka et al. 2012). Over the years, a number of automatic or semi-automatic segmentation approaches have been proposed in the literature (Mabrouk et al. 2012; Gutierrez et al. 2012; Lee et al. 2012; Katoh et al. 2012; Choy et al. 2011; Cheng-Liao & Qi 2010; Croteau et al. 2010; Maroy et al. 2008; El Fakhri et al. 2005; Liptrot et al. 2004; Brankov et al. 2003). Several of these methods need to estimate a priori the number of regions with homogeneous activities into which the image should be partitioned; a classic example of this is the k-means clustering algorithm (Duda et al. 2001).

However, in most cases this prior knowledge does not exist. In the case of the PET imaging technique, it is common to have several regions whose regional TACs are not homogeneous due

to contamination from a mixture of the activities of surrounding structures. Therefore, it makes sense to design a clustering approach that divides the image into as many regions with a similar kinetic behavior as needed, using a similarity metric to establish the threshold to create a new division. This process has been called *functional segmentation* (Rousset et al. 1998), to distinguish it from the classical segmentation solely based on morphological or structural considerations.

In this paper we present an open implementation of a clustering algorithm based on a leader-follower approach that groups voxels with similar TACs. This work extends and validates a preliminary implementation of this algorithm (Mateos-Pérez et al. 2011).

6.2 Materials and methods

6.2.1 Leader-follower algorithm definition and implementation

Let's consider every dynamic voxel in the image $\boldsymbol{v} = \{v_0, \ldots, v_{n-1}\}$ as a vector consisting of the sequence of different activity levels with time (t = {0, …, n-1}); this time vector is the TAC for that voxel. Also, consider a cluster $\boldsymbol{C}$ as a set of voxels, whose centroid $\boldsymbol{c}$ is the average activity for all the voxels in that set.

The classical leader-follower formulation applies the following steps (Duda et al. 2001) in order to complete the clustering operation:

1. Set a metric and a threshold.
2. Initialize the first cluster with the first voxel in the image.
3. Compute the metric between every voxel and each available cluster centroid. If the shortest computed metric is below the threshold, include that voxel in the corresponding cluster. If not, create a new cluster with that voxel.
4. Repeat until all the voxels have been included in a cluster.

The metric of choice is commonly the Euclidean distance, but since this distance may yield quite different values, it is more convenient for this particular algorithm to use a metric for which a known threshold can be set. For instance, it is possible to use the Pearson or Spearman correlation coefficients, or the cosine product, which have values bound in [-1, 1] and measure the similarity in shape between two given vectors. For this kind of metrics a voxel is included in a given cluster if the similarity measurement is above the threshold.

In the particular case of dynamic PET studies, two different tissues or organs may have similar TAC shapes but different activity levels. It is therefore interesting to build clusters with voxels that are not only similar in shape but also in amplitude. For this reason, we have modified the classical leader-follower algorithm by including additional the following steps, as follows:

1. Sort all the voxels in the image by comparing the amplitude. The ones with the greatest maximum amplitude are processed first.
2. Set a metric and a threshold. In this case, the cosine similarity metric is used, defined as

$$sim(\boldsymbol{v},\boldsymbol{c}) = \cos\theta = \frac{\boldsymbol{v}\cdot\boldsymbol{c}}{\|\boldsymbol{v}\|\cdot\|\boldsymbol{c}\|} \tag{6.1}$$

   where $\boldsymbol{v}$ and $\boldsymbol{c}$ are the voxel TAC vector and the centroid vector for cluster $\mathbf{C}$, respectively. This similarity metric computes the cosine of the angle between two given vectors and its values are bounded in [-1, 1], which allows the user to set a sensible and meaningful threshold.
3. Initialize the first cluster with the first voxel, following the sorted order.
4. Compute the similarity score between each voxel and the available clusters. If the similarity is above the given threshold, include that cluster in a set of candidates, $\mathbf{C_c}$. If no candidates are found, a that voxel is used to create a new cluster.
5. Select a cluster $\mathbf{C}_i$ from $\mathbf{C_c}$ such that

$$\arg\min_i D(\boldsymbol{v},\boldsymbol{c}_i)\cdot e^{-sim(\boldsymbol{v},\boldsymbol{c}_i)} \tag{6.2}$$

   where $D(\boldsymbol{v}, \boldsymbol{c}_i)$ is the Euclidean distance between the voxel TAC vector $\boldsymbol{v}$ and the centroid from cluster i. The exponential terms penalizes voxels close in amplitude to the centroid but less similar in shape.
6. Include the voxel in the selected cluster C_i.
7. Repeat until all voxels have been assigned.

Step 1 ensures that the next voxel to analyze is always the one with the largest amplitude available. This algorithm is very dependent on the order with which the voxels are processed for cluster creation, due to the fact that new clusters are created as needed when none of the already existing ones has the desired similarity scores. The initial sorting step helps optimizing the final result by forcing different clusters to include only those voxels with the greatest amplitude available among all that may have a similar shape, therefore minimizing the influence of noise and spill-over effects.

This algorithm has been implemented under the jClustering framework (Mateos-Pérez et al. 2013) for the ImageJ platform (Schneider et al. 2012) and has been released under a free software license (GPL). The source code, along with binary downloads, can be obtained at https://github.com/HGGM-LIM/jclustering/blob/master/src/main/java/jclustering/techniques/LeaderFollower.java.

6.2.2 Hardware and software specifications

The proposed algorithm has been included in jClustering v1.4.2 and has been tested under ImageJ v1.47r with Java 1.6.0_34 in a Windows 7 Professional operating system. The computer used to run the tests is a Dell Precision T1600, 8 GB RAM, with an Intel Xeon 3.1 GHz CPU.

6.2.3 Experimental protocol

Sixteen male NUDE NU/NU mice were used in this work. Animals were purchased from Charles River Laboratories (Spain), maintained at a constant temperature (24 ± 0.5ºC) under a 12h-hour light/dark cycle, and permitted free access to commercial rodent laboratory chow and water. All experimental animal procedures were conducted in conformity with the European Communities Council Directive 2010/63/EU and were approved by the Ethics Committee for Animal Experimentation of our Institution.

$1.5 \cdot 10^6$ CH-157MN human tumor cells were injected in both mouse flanks. Imaging was performed 7-21 days after tumor cell inoculation using a small-animal PET-CT scanner (ARGUS PET-CT, SEDECAL, Madrid). Scans were obtained under isoflurane anesthesia (3% induction and 1.5% maintenance in 100% O_2). Three different ^{68}Ga-DOTA-peptides (referred to in this paper as DOTA-A, DOTA-B and DOTA-C) were intravenously injected by the tail vein (mean activity 11.47 MBq, range 9.25 – 20.35 MBq). Tracer, day and mouse selection were randomized. As a mouse could be injected with more than one tracer more than one day, a total of 24 images were acquired.

6.2.4 Image acquisition and manual segmentation

Tracer injections were followed by a 90 minutes dynamic PET study. Dynamic data were reformatted into 112 time frames (20 x 10 s, 10 x 30 s and 82 x 60 s). Frames corresponding to the last 60 minutes of the study were summed to create a static image. Images were reconstructed using a 2D-OSEM (Ordered Subset Expectation Maximization) algorithm, providing images with 1.45 mm full width half maximum (FWHM) resolution (voxel size 0.3875 x 0.3875 x 0.7750 mm^3). Energy window was 400-700keV. Decay, deadtime and random corrections were applied.

CT images were acquired using the described PET/CT scanner using standard adequate parameters for tumor imaging: 320 mA, 45 KV, 360 projections, 8 shots, and 200 µm of resolution. CT images were reconstructed using a Feldkamp algorithm obtaining an isotropic

voxel size of 0.125 mm (Abella et al. 2012). These anatomical images did not require any registration with their corresponding PET scans thanks to the intrinsic alignment of the PET/CT device.

CT images were used to manually draw the regions of interest (ROI) for the tumors. The input function was obtained by manually delineating the descending aorta in the static PET image.

6.2.5 Automatic functional segmentation process

Prior to the segmentation of the studies, the image volume was masked to eliminate voxels outside the mouse body using a simple thresholding method.

The proposed leader-follower algorithm was applied to the resulting masked volume using different thresholds (0.4, 0.5, 0.6, 0.7 and 0.8). The centroids for the selected clusters were the TACs to be used as input for the Logan analysis.

6.2.6 Quantification

The volume of distribution was obtained for both the manual and the automatic segmentations. This kinetic parameter is a combination of individual rate parameters and is defined as

$$V_t = \frac{K_1}{k_2}\left(1 + \frac{k_3}{k_4}\right) \tag{6.3}$$

Kinetic analyses were carried out using standard graphical analysis for a two-tissue reversible compartmental model (Logan et al. 1990). The model was solved using the traceRkinetic modeling library (Mateos-Pérez et al. 2014).

6.2.7 Statistical analysis

In order to compare whether the automatic segmentations yielded results significantly different from the manual ones, paired Wilcoxon rank tests were carried out between the automatic and manual results within the same tracer. No multiple comparison correction was used for these tests.

Also, the differences in the volume of distribution for the different tracers within the same segmentation method, including the manual delineation, were tested. A non-parametric Kruskal-Wallis test was carried out to find differences between tracers, followed by a pairwise Wilcoxon rank test using the Bonferroni correction for multiple comparisons. Results were considered significant for $p < 0.05$.

Statistical analysis was done using the R statistical package v3.0.0 (R Core Team 2013).

6.3 Results

The automatic algorithm was successful in separating the desired regions when the threshold values were 0.6, 0.7 or 0.8 (Figure 6.1). Segmentation was not successful in some of the studies when the lowest threshold values were used (0.4 and 0.5), and no statistical results are reported here for these values. Figure 6.3 shows examples of the automatically obtained TACs along with the manual ones.

The total computation time employed by each algorithm and the final number of clusters created depending on the threshold are shown on Table 6.1.

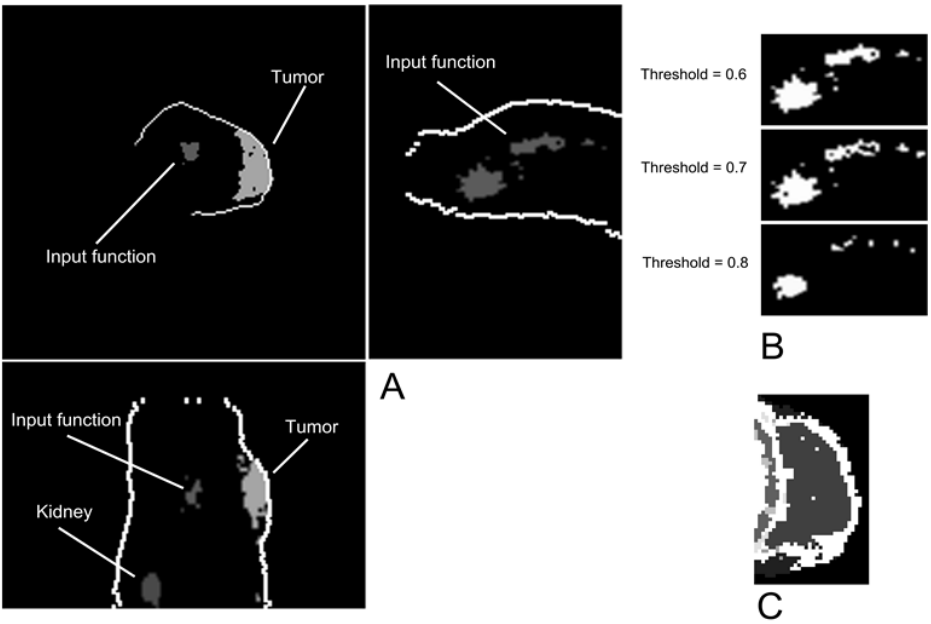

Figure 6.1: (A) Clustering results for one of the mouse studies analyzed in this work (threshold = 0.6). The regions belonging to the input function and the tumor have been selected; the kidneys have also been added to the final composition to show that the algorithm is able to segment different organs. (B) Effects of increasing the threshold value in the definition of the input function region (same region shown on Figure 1 (A)). As expected, as the threshold is increased, the cluster tends to concentrate in the center of the region, while the edges, heavily affected by spill-over, form their own clusters that can be discarded. (C) Detail of the tumoral region affected by spill-over from surrounding tissues. The window/level settings of the image have been set to clearly visualize the tumor region; surrounding clusters are shown on white color but they do not necessarily form a single connected region.

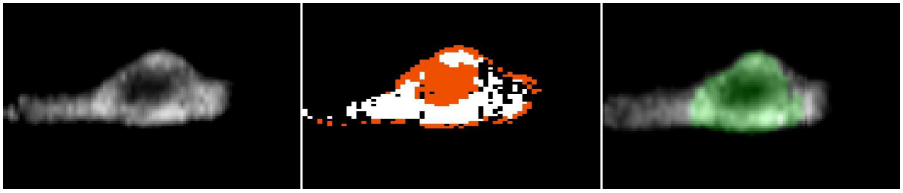

Figure 6.2: Sagittal slice of tumoral region: automatic segmentation has found two different regions, an area of necrotic tissue (low uptake) surrounded by high-uptake tissue, due to their different kinetics. Left: average image obtained by adding the last image frames in order to enhance tumoral tissue. Center: automatic segmentation for the necrotic tissue (red) and tumoral high-uptake tissue (white); threshold = 0.6. Right: manual ROI (green).

The results for the statistical analysis are summarized on Figure 6.4 and Table 6.2. No significant differences in the volume of distribution values were found within the same tracer between the manual region delineation and the automatic methods. The statistical analysis found significant differences (Kruskal-Wallis p-value = 0.0108) between DOTA-A and DOTA-B (p = 0.020) and DOTA-A and DOTA-C (p = 0.033) for the manual segmentation method; similar differences were found for all the automatic methods for which statistical results are reported (Kruskal-Wallis p-values for each threshold {0.6, 0.7 and 0.8} = 0.0019, 0.0023, 0.0013; refer to Figure 4 for pairwise p-values).

	Threshold 0.6	**Threshold 0.7**	**Threshold 0.8**
Time (s)	18.1 ± 4.8 (17.8)	26.3 ± 18.2 (22.2)	67.6 ± 92.9 (34.61)
# of clusters	149.5 ± 143.9 (102.5)	611.2 ± 820.8 (297)	2255.9 ± 2476.1 (1375.5)

Table 6.1. Total computation time (s), and number of clusters formed for each different threshold. Values are shown as mean ± standard deviation (median).

	Manual	**Threshold 0.6**	**Threshold 0.7**	**Threshold 0.8**
DOTA-A	0.45 ± 0.06	0.44 ± 0.07	0.46 ± 0.06	0.47 ± 0.05
DOTA-B	0.66 ± 0.16	0.72 ± 0.14	0.71 ± 0.12	0.71 ± 0.09
DOTA-C	0.63 ± 0.14	0.68 ± 0.15	0.69 ± 0.12	0.65 ± 0.10

Table 6.2. Volume of distribution values per tracer and segmentation method; p values are greater than the significance level (0.05) for the observed differences. V_t values are shown as mean ± standard deviation.

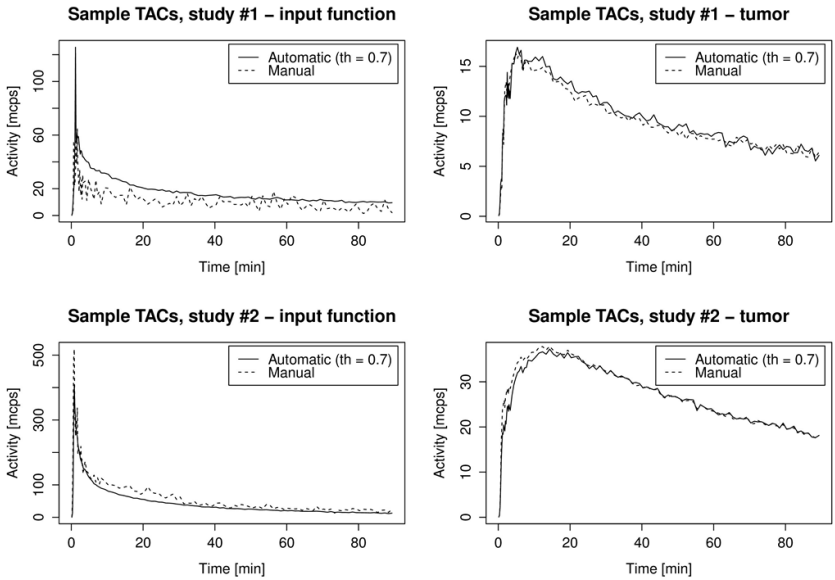

Figure 6.3: Example of TACs obtained with the automatic method and the manual delineation. Two different studies with different levels of activity are shown (the one with the lowest activity is shown at the top row).

6.4 Discussion

In this paper we present a novel segmentation algorithm based on a leader-follower approach that, instead of setting a priori a number for the final number of clusters, creates as many as needed depending on a similarity threshold set by the user. In our tests, the algorithm successfully extracted the TACs for the relevant tissues or regions when the threshold was above a certain critical value. Studies with lower injected activity, which tend to be more affected by noise, were separated into more clusters for the same threshold value. This approach ensures the basic assumption of kinetic analysis, which is the homogeneous kinetic behavior of the voxels assigned to a particular region (Morris et al. 2004; Takesh 2012).

Our algorithm addresses one of the weaknesses of the k-means algorithm, in which the user needs to run the algorithm several times before reaching an optimal solution due to the random initialization step (Zanotti-Fregonara et al. 2009). From this perspective, our algorithm ensures the reproducibility of the segmentation results and provides a result that does not change for each run.

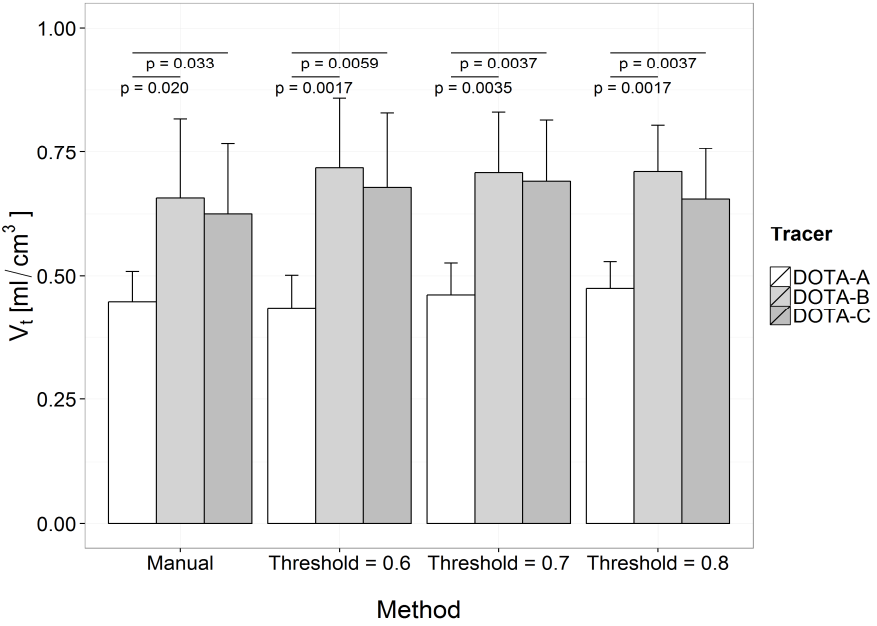

Figure 6.4: Volumes of distribution for different segmentation procedures (manual, automatic with different thresholds). P-values within the same segmentation method are adjusted for multiple comparisons using the Bonferroni correction.

The volume of distribution has been chosen as the parameter used to compare the goodness of the different segmentations for two reasons. Firstly, the initial experiment used that parameter to measure the binding of the different tracers to the tumors, and the automatic segmentation aims at replicating the manual results. Secondly, the volume of distribution is computed using the individual kinetic rate parameters (as shown on Equation 1.3) and the error resulting from the linear fit is smaller than those obtained for each of the individual components using non-linear methods. This parameter has been used previously in the literature for similar algorithm validation purposes (Lyoo et al. 2014).

Regarding the volume of distribution obtained with the automatically segmented TACs, we confirmed that the algorithm is stable: the variation of the threshold value does not cause significant changes in the volume of distribution for each tracer (Figure 6.4), since the differences between the tracers and the sign of those differences are maintained. As this threshold value is increased, the variability of the volume of distribution decreases. We hypothesize that this is due to the reduction in the region size obtained when the similarity threshold is increased (Figure 6.1 (B)), therefore decreasing TAC heterogeneity due to partial

volume effects or noise, as the area included in the cluster is concentrated on the center of the region, where voxels are less mixed with activity from surrounding organs or tissues (Maroy et al. 2008). This effect is clearly seen in Figure 6.1 (C), where the tumor region is surrounded by smaller clusters heavily affected by spill-over. Those small clusters are not included in the segmented tissue because their TACs do not conform to the similarity or distance constrains imposed by the algorithm.

While the manually segmented regions and the automatic ones tended to overlap (Figure 6.2), they are not identical. Some of the segmented tumors show internal heterogeneity, often being divided into high-uptake and low-uptake regions, probably caused by necrosis. As the tumor ROIs were manually drawn over the CT image, where they appear homogeneous, these functional differences were not taken into account, and in some cases necrotic tissue, usually present in the center of the tumor region, was included. This higher sensitivity of the automatic method may account for the slightly higher overall volume of distribution values (Table 6.2), as the tumor TAC has been extracted using only the high-uptake areas. This manual segmentation error is shared among the different tracers and its overall effect can be disregarded if the final objective is to evaluate which tracer has the greater uptake in the tumoral tissue. However, it can be an important detail to consider when the quantification measurements need a precise result that accounts faithfully for the volume of distribution in the active tumor; in this respect, the same regions of interest could have been drawn using the summed PET image. Also, it is a common practice to obtain the input function from a very small region to minimize as much as possible the influence of spillover. In that respect, when the segmentation process aims at extracting the TAC for each tissue, region overlapping is not as useful as the kinetic analysis results when comparing automatic segmentation algorithms with a manual process.

This work has a number of limitations. The algorithm does not include any partial volume or spill-over correction logic, such as GTM (Rousset et al. 2008), but this is not its primary purpose, as it is intended to replicate the results obtained from a manual segmentation. While in the small animal studies used in this work there was no blood sampling and therefore the volumes of distribution values are potentially biased, the validation carried out proves that both the manual and the automatic segmentation yield TACs that lead to equivalent results.

Also, the similarity threshold may take arbitrary values and, even if its mathematical meaning is clear, the practical result is subject to a process of trial and error, as the final number of clusters depends on a number of factors, including the image noise. In any case, as the algorithm is fast, different values can be tested until the relevant structures can be discerned via visual inspection. Table 6.2 shows the computation times and number of clusters created. A high threshold value (i.e. 0.8) over-segments the data, but most of the created clusters have a size of just a few pixels and can be discarded as noise. Furthermore, as the algorithm presents the results so that larger clusters are shown first, it is easy to locate the relevant organs in the user interface. Figure 6.1 (B) shows that high values also cause the final result to stay closer to the region center, so a

balance needs to be achieved: larger threshold values imply more concentrated clusters but also more fragmentation.

Although in this work we have validated the algorithm using the cosine similarity metric, other similarity metrics, such as the Pearson correlation score or the Spearman rank correlation coefficient, have also been implemented and have shown similar results in preliminary tests, but the computation times were higher.

6.5 Conclusion

We present an open implementation of a segmentation algorithm for dynamic PET studies based on grouping voxels with similar TACs. Automatic segmentation successfully replicates the manual results obtained in small animal studies, therefore becoming a reliable substitute for this task and potentially for other dynamic segmentation procedures. This algorithm based on a leader-follower approach is fast, the source code is publicly available and can be directly used from the ImageJ image analysis and processing platform.

7 Conclusions

The main contributions and conclusions of this PhD thesis are the following:

1. A novel supervised clustering algorithm was developed and tested on a set of three swine $^{13}NH_3$ studies. This algorithm is based on iterative correlation measurements done on curves of known shape using a leave-one-out cross-validation schema for the training process. Tests showed that this approach can be successfully used, provided the image test set has similar temporal behavior. This method diminished the error in the estimated rate parameters resulting from the two-compartment non-linear fitting process compared to the manual segmentation. The myocardium TAC obtained with this method has smaller spill-over than the one obtained from the manual delineation. The source code for this PMOD plugin is available at https://github.com/HGGM-LIM/j.cmpb.2013.04.010.

2. A novel algorithm based on a leader-follower approach, modified specifically for the purpose of dynamic PET functional segmentation, was proposed and openly implemented under jClustering. This method modified the classical algorithm so that a user-defined threshold for similarity scores (cosine) and a Euclidean TAC distance were both taken into consideration when grouping voxels with similar activities. It was shown that this algorithm was able to successfully perform TAC extraction from a series of 24 images obtained from 16 rodent studies. The posterior quantification yielded the same kinetic parameters as the manual delineation. The tests carried out showed that it may provide a more precise segmentation for structures that look anatomically homogeneous but that internally show different kinetic behaviors. The source code for this algorithm can be downloaded at http://bit.ly/leader-follower-jclustering.

3. jClustering, a Java framework designed for the implementation of clustering algorithms on dynamic images, has been developed and published as a free and open source project. This software project provides a tool that can be used to easily implement new 4D (3D + time) clustering algorithms in such a way that the tools can be shared to ensure study reproducibility. The most commonly used algorithms have been implemented and this tool has been also used to develop the novel leader-follower algorithm presented in this thesis. Its source code and binary downloads are available at https://github.com/HGGM-LIM/jclustering.

4. Other auxiliary software was also developed and released as a free or open source projects. Especially worth mentioning is traceRkinetic, an R library for kinetic modeling that includes the most commonly used models. Several of those models have been validated against the PMOD commercial software. It can be downloaded in both binary and source formats at https://github.com/HGGM-LIM/tracerkinetic.

8 Publications

8.1 Directly related to this thesis

8.1.1 Articles in peer-reviewed journals

J. M. Mateos-Pérez, M. L Soto-Montenegro, S. Peña-Zalbidea, M. Desco and J. J. Vaquero, "Automatic functional segmentation of dynamic PET studies: a leader-follower-based algorithm open source implementation and validation," (submitted).

M. L. Soto-Montenegro, S. Peña-Zalbidea, **J. M. Mateos-Pérez**, M. Oteo, E. Romero, M. A. Morcillo, M. Desco. "Comparison of ^{68}Ga-DOTATOC, ^{68}Ga-DOTANOC and ^{68}Ga-DOTATATE for molecular imaging in mice bearing meningioma tumors," (in preparation).

J. M. Mateos-Pérez, C. García-Villalba, J. Pascau, M. Desco, and J. J. Vaquero, "jClustering, an Open Framework for the Development of 4D Clustering Algorithms," *PLoS ONE*, vol. 8, no. 8, p. e70797, 2013.

J. M. Mateos-Pérez, M. Desco, M. W. Dae, C. García-Villalba, L. Cussó, and J. J. Vaquero, "Automatic TAC extraction from dynamic cardiac PET imaging using iterative correlation from a population template," *Computer Methods and Programs in Biomedicine*, vol. 111, no. 2, pp. 308–314, 2013.

8.1.2 International conferences

J. M. Mateos-Pérez, M. Desco, and J. J. Vaquero, "Tracer Kinetic Modeling with R for Batch Processing of Dynamic PET Studies," in *XIII Mediterranean Conference on Medical and Biological Engineering and Computing 2013 SE - 75*, 2014, vol. 41, pp. 301–304.

E. E. Greenblatt, **J. M. Mateos-Pérez**, T. Winkler, V. J. Kelly, R. S. Harris, and J. G. Venegas, "Anatomic Distribution Of Aerosol Deposition In Bronchoconstricted Subjects With Asthma," in *American Thoracic Society International Conference*, 2012, pp. A5623–A5623.

J. M. Mateos-Pérez, J. J. Vaquero, C. García-Villalba, L. Cussó, and M. Desco, "Leader-follower clustering algorithm for automatic segmentation of cardiac PET studies," in *2011 IEEE Nuclear Science Symposium Conference Record*, 2011, pp. 3133–3136.

J. M. Mateos-Pérez, C. García-Villalba, M. Dae, M. Abella, M. Desco, and J. J. Vaquero, "Iterative automatic segmentation in cardiac PET based on TAC correlation: Preliminary results," in *IEEE Nuclear Science Symposium & Medical Imaging Conference*, 2010, pp. 2084–2087.

8.1.3 National conferences

J. M. Mateos-Pérez, C. García-Villalba, J. Pascau, M. Desco, and J. J. Vaquero, "jClustering, un entorno de código libre para ImageJ para el desarrollo de algoritmos de clustering aplicados a segmentación de imágenes médicas dinámicas," in Libro de Actas XXX CASEIB 2012, 2012.

J. M. Mateos-Pérez, C. García-Villalba, L. Cussó, M. Desco, and J. J. Vaquero, "Clustering leader-follower para la segmentación automática de estudios PET cardíacos," in Libro de actas del XXIX Congreso Anual de la Sociedad Española de Ingeniería Biomédica (CASEIB), 2011, pp. 67–69.

J. M. Mateos-Pérez, C. García-Villalba, M. Abella, M. Desco, and J. J. Vaquero, "Segmentación automática de estudios PET cardíacos con $^{13}NH_3$ basada en correlación iterativa," in Proceedings del XXVIII Congreso Anual de la Sociedad Española de Ingeniería Biomédica (CASEIB), 2010.

8.2 Other publications

8.2.1 Articles in peer-reviewed journals

M. Lacalle-Aurioles, **J. M. Mateos-Pérez**, J. A. Guzmán-De-Villoria, J. Olazarán, I. Cruz-Orduña, Y. Alemán-Gómez, M.-E. Martino, and M. Desco, "Cerebral blood flow is an earlier indicator of perfusion abnormalities than cerebral blood volume in Alzheimer's disease.," *J. Cereb. Blood Flow Metab.*, vol. 34, no. 4, pp. 654–659, 2014.

M. Lacalle-Aurioles, Y. Alemán-Gómez, J. A. Guzmán-De-Villoria, I. Cruz-Orduña, J. Olazarán, **J. M. Mateos-Pérez**, M. E. Martino, and M. Desco, "Is the cerebellum the optimal reference region for intensity normalization of perfusion MR studies in early Alzheimer's disease?," *PLoS One*, vol. 8, no. 12, p. e81548, 2013.

J. M. Mateos-Pérez, R. Redondo, R. Nava, J. C. Valdiviezo, G. Cristóbal, B. Escalante-Ramírez, M. J. Ruiz-Serrano, J. Pascau, and M. Desco, "Comparative evaluation of autofocus algorithms for a real-time system for automatic detection of Mycobacterium tuberculosis.," *Cytometry. A*, vol. 81, no. 3, pp. 213–21, 2012.

J. Janssen, Y. Alemán-Gómez, S. Reig, H. G. Schnack, M. Parellada, M. Graell, C. Moreno, D. Moreno, **J. M. Mateos-Pérez**, J. M. Udias, C. Arango, and M. Desco, "Regional specificity of thalamic volume deficits in male adolescents with early-onset psychosis.," *Br. J. Psychiatry*, vol. 200, no. 1, pp. 30–6, 2012.

J. A. Guzmán-De-Villoria, P. Fernández-García, **J. M. Mateos-Pérez**, and M. Desco, Estudio de la perfusión cerebral mediante técnicas de susceptibilidad magnética: técnica y aplicaciones" *Radiología*, vol. 54, no. 3, pp. 208–20, 2012.

J. Janssen, Y. Alemán, S. Reig, H. Schnack, M. Parellada, M. Graell, C. Moreno, D. Moreno, **J. M. Mateos-Pérez**, and J. M. Udias, "Thalamus volume and shape in male adolescents with early-onset first-episode psychosis," *Schizophr. Res.*, vol. 117, no. 2–3, pp. 203–203, 2010.

8.2.2 International conferences

M. Lacalle-Aurioles, Y. Alemán-Gómez, J. Guzmán-De-Villoria, J. Olazarán, I. Cruz, **J. M. Mateos-Pérez**, M. E. Martino, and M. Desco, "The Importance of a Valid Reference Region for Intensity Normalization of Perfusion MR Studies in Early Alzheimer's Disease," in *XIII Mediterranean Conference on Medical and Biological Engineering and Computing 2013 SE - 54*, vol. 41, L. M. Roa Romero, Ed. Springer International Publishing, 2014, pp. 218–220.

J. A. Guzmán-De-Villoria, **J. M. Mateos-Pérez**, P. Fernández-García, P. Borrego-Ruiz, and M. Desco, "Differentiation between Gliomas and Brain Metastases Using MR Imaging, Resonance Spectroscopy, Perfusion and Diffusion-Weighted Imaging," in *Proceedings of the ASNR 51st Annual Meeting*, 2013, p. 115.

J. M. Mateos-Pérez, J. A. Guzmán-De-Villoria, I. Vidal, and M. Desco, "Diagnostic value of brain functional imaging in the assessment of intraaxial tumors," in *Proceedings of the International Society of Magnetic Resonance in Medicine*, 2009, p. 1001.

S. Reig, J. A. Guzmán-De-Villoria, J. Olazarán, M. Lacalle-Aurioles, M.-E. Martino, **J. M. Mateos-Pérez**, I. Cruz-Orduña, V. García, and M. Desco, "Choice of reference region for the normalization of brain Cerebral Blood Volume maps in comparative studies," in *Neuroimage*, 2009, p. S125.

J. M. Mateos-Pérez, V. Garcia-Vázquez, J. Sánchez-González, J. Pascau González-Garzón, J. A. Guzmán-De-Villoria, S. Reig, and M. Desco, "Development and benchmarking of a quantification tool for cerebral MR perfusion studies," in *International Journal of Computer Assisted Radiology and Surgery*, 2008, p. S358.

8.2.3 National conferences

F. Alfaro-Almagro, Y. Alemán-Gómez, **J. M. Mateos-Pérez**, J. Janssen, J. Pascau, and M. Desco, "Plataforma cloud de procesamiento paralelo de neuroimagen usando virtualización," in *CASEIB 2012*, 2012.

J. M. Mateos-Pérez, J. Pascau González-Garzón, and M. Desco, "Recursos informáticos para la gestión de un laboratorio de ingeniería biomédica," in *Proceedings del XXVIII Congreso Anual de la Sociedad Española de Ingeniería Biomédica (CASEIB)*, 2010.

M. Lacalle-Aurioles, S. Reig, J. A. Guzmán-De-Villoria, **J. M. Mateos-Pérez**, J. Olazarán, I. Cruz-Orduña, M.-E. Martino, J. Navas, V. Rebollo, L. Sánchez, and M. Desco, "Normalización

de datos de perfusión por RM: resultados contradictorios en las diferencias entre pacientes de Alzheimer y controles dependiendo de la región de referencia," in *Libro de Resúmenes del CASEIB 2009*, 2009, pp 141.

J. M. Mateos-Pérez, M. J. Ruiz-Serrano, T. Peláez-García, J. Pascau González-Garzón, and M. Desco, "Algoritmos de autoenfoque para un sistema de detección automática de bacilos," in *Libro de Resúmenes del CASEIB 2009*, 2009, p. 139.

J. M. Mateos-Pérez, I. Vidal, J. A. Guzmán-De-Villoria, and M. Desco, "Desarrollo de un clasificador de tumores cerebrales," in *Libro de Actas del CASEIB 2008*, 2008, pp. 407–410.

J. M. Mateos-Pérez, V. García, J. Sánchez-González, J. Pascau González-Garzón, J. A. Guzmán-De-Villoria, S. Reig, and M. Desco, "Comparativa entre herramientas de cuantificación de estudios de perfusión por resonancia magnética," in *Actas del XXV Congreso Anual de la Sociedad Española de Ingeniería Biomédica*, 2007, pp. 519–522.

J. M. Mateos-Pérez, V. García, J. Sánchez-González, J. Pascau González-Garzón, J. A. Guzmán-De-Villoria, S. Reig, and M. Desco, "Herramienta de Cuantificación de Estudios de Perfusión por Resonancia Magnética," in *Libro de Actas, CASEIB 2006*, 2006, pp. 301–304.

8.2.4 Books

J. M. Mateos-Pérez and J. Pascau, *Image processing with ImageJ*. Packt Publishing, 2013.

9 References

Abella, M. et al., 2012. Software architecture for multi-bed FDK-based reconstruction in X-ray CT scanners. *Computer Methods and Programs in Biomedicine*, 107, pp.218–232.

Arganda-Carreras, I. et al., 2013. Trainable Weka Segmentation. *Fiji website*. Available at: http://fiji.sc/Trainable_Weka_Segmentation [Accessed July 17, 2013].

Arthur, D. & Vassilvitskii, S., 2007. k-means++: the advantages of careful seeding. In *Proceedings of the eighteenth annual ACM-SIAM symposium on Discrete algorithms*. Philadelphia, PA, USA: Society for Industrial and Applied Mathematics, pp. 1027–1035.

Bacharach, S.L. & Carson, R.E., 2013. In hot blood: quantifying the arterial input function. *JACC. Cardiovascular imaging*, 6(5), pp.569–73.

Bailey, D.L. et al. eds., 2003. *Possitron Emission Tomography*, Springer.

Barber, D.C., 1980. The use of principal components in the quantitative analysis of gamma camera dynamic studies. *Physics in medicine and biology*, 25(2), pp.283–92.

Barnes, N., 2010. Publish your computer code: it is good enough. *Nature*, 467(7317), p.753.

Beller, G. a & Bergmann, S.R., 2004. Myocardial perfusion imaging agents: SPECT and PET. *Journal of nuclear cardiology : official publication of the American Society of Nuclear Cardiology*, 11(1), pp.71–86.

Bentourkia, M. et al., 1999. A standardized blood sampling scheme in quantitative FDG-PET studies. *IEEE transactions on medical imaging*, 18(5), pp.379–84.

Boudraa, A.O. et al., 1999. Analysis of dynamic nuclear cardiac images by covariance function. *Computerized medical imaging and graphics : the official journal of the Computerized Medical Imaging Society*, 23(4), pp.181–91.

Brankov, J.G., Galatsanos, N.P. & Wernick, M.N., 2003. Segmentation of Dynamic PET or fMRI Images Based on a Similarity Metric. *IEEE Transactions on Nuclear Science*, 50(5), pp.1410–1414.

Case, J. & Bateman, T., 2013. Taking the perfect nuclear image: Quality control, acquisition, and processing techniques for cardiac SPECT, PET, and hybrid imaging. *Journal of Nuclear Cardiology*, pp.1–17.

Chen, K. et al., 1998. Noninvasive Quantification of the Cerebral Metabolic Rate for Glucose Using Positron Emission Tomography, 18F-Fluoro-2-Deoxyglucose, the Patlak Method, and an Image-Derived Input Function. *J Cereb Blood Flow Metab*, 18(7), pp.716–723.

Cheng-Liao, J. & Qi, J., 2010. Segmentation of mouse dynamic PET images using a multiphase level set method. *Physics in medicine and biology*, 55(21), pp.6549–69.

Choy, S., Tang, M. & Tong, C., 2011. Image Segmentation Using Fuzzy Region Competition and Spatial/Frequency Information. *Image Processing, IEEE Transactions on*, 20(99), pp.1473–1484.

Croteau, E. et al., 2010. Image-derived input function in dynamic human PET/CT: methodology and validation with 11C-acetate and 18F-fluorothioheptadecanoic acid in muscle and 18F-fluorodeoxyglucose in brain. *European journal of nuclear medicine and molecular imaging*, 37(8), pp.1539–50.

DeGrado, T.R. et al., 1996. Estimation of myocardial blood flow for longitudinal studies with 13N-labeled ammonia and positron emission tomography. *Journal of nuclear cardiology : official publication of the American Society of Nuclear Cardiology*, 3(6 Pt 1), pp.494–507.

Dekemp, R.A. et al., 2013. Multisoftware Reproducibility Study of Stress and Rest Myocardial Blood Flow Assessed with 3D Dynamic PET/CT and a 1-Tissue-Compartment Model of 82Rb Kinetics. *Journal of nuclear medicine : official publication, Society of Nuclear Medicine*, 54, pp.571–577.

Dewalle-Vignion, A.-S. et al., 2011. Evaluation of PET volume segmentation methods: comparisons with expert manual delineations. *Nuclear medicine communications*.

Duda, R.O., Hart, P.E. & Stork, D.G., 2001. *Pattern Classification*, Wiley-Interscience.

Elzhov, T. V et al., 2012. minpack.lm: R interface to the Levenberg-Marquardt nonlinear least-squares algorithm found in MINPACK, plus support for bounds.

El Fakhri, G. et al., 2005. Quantitative dynamic cardiac 82Rb PET using generalized factor and compartment analyses. *Journal of nuclear medicine : official publication, Society of Nuclear Medicine*, 46(8), pp.1264–71.

Flotats, A. et al., 2012. (82)Rb PET myocardial perfusion imaging is superior to (99m)Tc-labelled agent SPECT in patients with known or suspected coronary artery disease. *European journal of nuclear medicine and molecular imaging*.

Fung, E.K. & Carson, R.E., 2013. Cerebral blood flow with [(15)O]water PET studies using an image-derived input function and MR-defined carotid centerlines. *Physics in medicine and biology*, 58(6), pp.1903–23.

De Geus-Oei, L.-F. et al., 2006. Comparison of image-derived and arterial input functions for estimating the rate of glucose metabolism in therapy-monitoring 18F-FDG PET studies. *Journal of nuclear medicine : official publication, Society of Nuclear Medicine*, 47(6), pp.945–9.

Gunn, R.N. et al., 2002. Positron Emission Tomography Compartmental Models: A Basis Pursuit Strategy for Kinetic Modeling. *Journal of Cerebral Blood Flow & Metabolism*, 22(12), pp.1425–1439.

Gunn, R.N., Gunn, S.R. & Cunningham, V.J., 2001. Positron emission tomography compartmental models. *Journal of cerebral blood flow and metabolism : official journal of the International Society of Cerebral Blood Flow and Metabolism*, 21(6), pp.635–52.

Guo, H. et al., 2003. Clustering huge data sets for parametric PET imaging. *Biosystems*, 71(1-2), pp.81–92.

Gutierrez, D. et al., 2012. Anatomically guided voxel-based partial volume effect correction in brain PET: Impact of MRI segmentation. *Computerized medical imaging and graphics : the official journal of the Computerized Medical Imaging Society*, pp.1–10.

Hall, M. et al., 2009. The WEKA data mining software. *ACM SIGKDD Explorations Newsletter*, 11(1), p.10.

Hapdey, S. et al., 2011. Searching for alternatives to full kinetic analysis in 18F-FDG PET: an extension of the simplified kinetic analysis method. *Journal of nuclear medicine : official publication, Society of Nuclear Medicine*, 52(4), pp.634–41.

Hastie, T., Tibshirani, R. & Friedman, J., 2009. *The Elements of Statistical Learning*, Springer.

Hermansen, F. et al., 1998. Measurement of myocardial blood flow with oxygen-15 labelled water: comparison of different administration protocols. *Eur J Nucl Med*, 25, pp.751–9 ST – Measurement of myocardial blood flow w.

Hostetler, E.D. et al., 2012. Evaluation of [(18)F]MK-0911, a Positron Emission Tomography (PET) Tracer for Opioid Receptor-Like 1 (ORL1), in Rhesus Monkey and Human. *NeuroImage*.

Huang, S.C. et al., 1980. Noninvasive determination of local cerebral metabolic rate of glucose in man. *The American journal of physiology*, 238(1), pp.E69–82.

Huisman, M.C. et al., 2012. Cerebral blood flow and glucose metabolism in healthy volunteers measured using a high-resolution PET scanner. *EJNMMI Research*, 2(1), p.63.

Ichise, M. et al., 2002. Strategies to improve neuroreceptor parameter estimation by linear regression analysis. *Journal of Cerebral Blood …*, 22, pp.1271–1281.

Ikoma, Y. et al., 2008. PET kinetic analysis: error consideration of quantitative analysis in dynamic studies. *Annals of nuclear medicine*, 22(1), pp.1–11.

Ince, D.C., Hatton, L. & Graham-Cumming, J., 2012. The case for open computer programs. *Nature*, 482(7386), pp.485–8.

Innis, R.B. et al., 2007. Consensus nomenclature for in vivo imaging of reversibly binding radioligands. *Journal of cerebral blood flow and metabolism : official journal of the International Society of Cerebral Blood Flow and Metabolism*, 27(9), pp.1533–9.

Katoh, C. et al., 2012. Quantification of regional myocardial blood flow estimation with three-dimensional dynamic rubidium-82 PET and modified spillover correction model. *Journal of nuclear cardiology : official publication of the American Society of Nuclear Cardiology*.

Kim, J. et al., 2006. Minimally invasive method of determining blood input function from PET images in rodents. *Journal of nuclear medicine : official publication, Society of Nuclear Medicine*, 47(2), pp.330–6.

Kim, J. et al., 2006. Segmentation of VOI from multidimensional dynamic PET images by integrating spatial and temporal features. *IEEE Transactions on Information Technology in Biomedicine*, 10(4), pp.637–46.

Kim, S.J. et al., 2008. Multiple linear analysis methods for the quantification of irreversibly binding radiotracers. *Journal of cerebral blood flow and metabolism : official journal of the International Society of Cerebral Blood Flow and Metabolism*, 28(12), pp.1965–77.

Kimura, Y. et al., 2007. PET kinetic analysis --pitfalls and a solution for the Logan plot. *Annals of nuclear medicine*, 21(1), pp.1–8.

Klein, R. et al., 2008. Model-based factor analysis of dynamic sequences of cardiac positron emission tomography. In *Nuclear Science Symposium Conference Record, 2008. NSS '08. IEEE*. pp. 5198–5202.

Krivokapich, J. et al., 1989. 13N ammonia myocardial imaging at rest and with exercise in normal volunteers. Quantification of absolute myocardial perfusion with dynamic positron emission tomography. *Circulation*, 80(5), pp.1328–1337.

Lee, J.S. et al., 1999. Robust extraction of input function from H215O dynamic myocardial positron emission tomography using independent component analysis. *IEEE Nuclear Science Symposium Conference Record.*, pp.990–994.

Lee, J.-S. et al., 2012. Extraction of an input function from dynamic micro-PET images using wavelet packet based sub-band decomposition independent component analysis. *NeuroImage*.

Liptrot, M. et al., 2004. Cluster analysis in kinetic modelling of the brain: a noninvasive alternative to arterial sampling. *NeuroImage*, 21(2), pp.483–493.

Logan, J. et al., 1990. Graphical analysis of reversible radioligand binding from time-activity measurements applied to [N-11C-methyl]-(-)-cocaine PET studies in human subjects.

Journal of cerebral blood flow and metabolism : official journal of the International Society of Cerebral Blood Flow and Metabolism, 10(5), pp.740–7.

Lortie, M. et al., 2007. Quantification of myocardial blood flow with 82Rb dynamic PET imaging. *European journal of nuclear medicine and molecular imaging*, 34(11), pp.1765–74.

Lyoo, C.H. et al., 2014. Image-derived input function derived from a supervised clustering algorithm: methodology and validation in a clinical protocol using [(11)c](R)-rolipram. K. Herholz, ed. *PloS one*, 9(2), p.e89101.

Mabrouk, R., Dubeau, F. & Bentabet, L., 2012. Dynamic Cardiac PET Imaging : Extraction of Time-Activity Curves using ICA and a Generalized Gaussian Distribution Model. *IEEE Transactions on Biomedical Engineering*, PP(99).

Magadán-Méndez, M. et al., 2010. ICA based automatic segmentation of dynamic H(2)(15)O cardiac PET images. *IEEE transactions on information technology in biomedicine*, 14(3), pp.795–802.

Maroy, R. et al., 2010. Quantitative organ time activity curve extraction from rodent PET images without anatomical prior. *Medical Physics*, 37(4), p.1507.

Maroy, R. et al., 2008. Segmentation of rodent whole-body dynamic PET images: an unsupervised method based on voxel dynamics. *IEEE Transactions on Medical Imaging*, 27(3), pp.342–54.

Mateos-Pérez, J.M. et al., 2013. jClustering, an Open Framework for the Development of 4D Clustering Algorithms L. Martens, ed. *PLoS ONE*, 8(8), p.e70797.

Mateos-Pérez, J.M. et al., 2011. Leader-follower clustering algorithm for automatic segmentation of cardiac PET studies. In *2011 IEEE Nuclear Science Symposium Conference Record*. IEEE, pp. 3133–3136.

Mateos-Pérez, J.M., Desco, M. & Vaquero, J.J., 2014. Tracer Kinetic Modeling with R for Batch Processing of Dynamic PET Studies. In L. M. Roa Romero, ed. *XIII Mediterranean Conference on Medical and Biological Engineering and Computing 2013 SE - 75*. Springer International Publishing, pp. 301–304.

Meyer, P.T. et al., 2006. Simplified quantification of small animal [18F]FDG PET studies using a standard arterial input function. *European journal of nuclear medicine and molecular imaging*, 33(8), pp.948–54.

Morris, E.D. et al., 2004. Kinetic Modeling in Positron Emission Tomography. In *Emission Tomography: The Fundamentals of PET and SPECT*. Elsevier, pp. 499–540.

Mourik, J.E.M. et al., 2009. Image-derived input functions for PET brain studies. *European journal of nuclear medicine and molecular imaging*, 36(3), pp.463–71.

Mouysset, S. et al., 2013. Segmentation of dynamic PET images with kinetic spectral clustering. *Physics in medicine and biology*, 58(19), pp.6931–6944.

O'Sullivan, F. et al., 2010. Kinetic quantitation of cerebral PET-FDG studies without concurrent blood sampling: statistical recovery of the arterial input function. *IEEE transactions on medical imaging*, 29(3), pp.610–24.

Pain, F. et al., 2004. Arterial input function measurement without blood sampling using a beta-microprobe in rats. *Journal of nuclear medicine : official publication, Society of Nuclear Medicine*, 45(9), pp.1577–82.

Di Paola, R. et al., 1982. Handling of Dynamic Sequences in Nuclear Medicine. *IEEE Transactions on Nuclear Science*, 29(4), pp.1310–1321.

Parker, B.J., 2005. Graph-based Mumford-Shah segmentation of dynamic PET with application to input function estimation. *Nuclear Science, IEEE Transactions on*, 52(1), pp.79–89.

Patlak, C., Blasberg, R. & Fenstermacher, J., 1983. Graphical evaluation of blood-to-brain transfer constants from multiple-time uptake data. *J Cereb Blood Flow Metab*.

Pedersen, F. et al., 1994. Principal component analysis of dynamic positron emission tomography images. *European journal of nuclear medicine*, 21(12), pp.1285–92.

Pérez-Campaña, C. et al., 2013. Assessing Lung Inflammation After Nanoparticle Inhalation Using 2-deoxy-2-[(18)F]fluoro-D-glucose Positron Emission Tomography Imaging. *Molecular imaging and biology : MIB : the official publication of the Academy of Molecular Imaging*.

Prieto, E. et al., 2012. Twelve automated thresholding methods for segmentation of PET images: a phantom study. *Physics in medicine and biology*, 57(12), pp.3963–3980.

R Core Team, 2013. R: A Language and Environment for Statistical Computing.

Rahmim, A. & Zaidi, H., 2008. PET versus SPECT: strengths, limitations and challenges. *Nuclear medicine communications*, 29(3), pp.193–207.

Razifar, P. et al., 2006. A new application of pre-normalized principal component analysis for improvement of image quality and clinical diagnosis in human brain PET studies--clinical brain studies using [11C]-GR205171, [11C]-L-deuterium-deprenyl, [11C]-5-Hydroxy-L-Tryptophan, [11. *NeuroImage*, 33(2), pp.588–98.

Razifar, P. et al., 2009. An automated method for delineating a reference region using masked volumewise principal-component analysis in 11C-PIB PET. *Journal of nuclear medicine technology*, 37(1), pp.38–44.

Rousset, O.G. et al., 2008. Design and implementation of an automated partial volume correction in PET: application to dopamine receptor quantification in the normal human

striatum. *Journal of nuclear medicine : official publication, Society of Nuclear Medicine*, 49(7), pp.1097–106.

Rousset, O.G., Ma, Y. & Evans, A.C., 1998. Correction for partial volume effects in PET: principle and validation. *Journal of Nuclear Medicine*, 39(5), p.904.

Schain, M. et al., 2013. Arterial input function derived from pairwise correlations between PET-image voxels. *Journal of cerebral blood flow and metabolism : official journal of the International Society of Cerebral Blood Flow and Metabolism*, (February), pp.1–8.

Schindelin, J. et al., 2012. Fiji: an open-source platform for biological-image analysis. *Nature methods*, 9(7), pp.676–82.

Schneider, C.A., Rasband, W.S. & Eliceiri, K.W., 2012. NIH Image to ImageJ: 25 years of image analysis. *Nature Methods*, 9(7), pp.671–675.

Schroeder, T. et al., 2007. Image-Derived Input Function for Assessment of 18F-FDG Uptake by the Inflamed Lung. *J Nucl Med*, 48(11), pp.1889–1896.

Sitek, A., Gullberg, G.T. & Huesman, R.H., 2002. Correction for ambiguous solutions in factor analysis using a penalized least squares objective. *IEEE Transactions on Medical Imaging*, 21(3), pp.216–25.

Slomka, P.J. et al., 2012. Comparison of clinical tools for measurements of regional stress and rest myocardial blood flow assessed with 13N-ammonia PET/CT. *Journal of nuclear medicine : official publication, Society of Nuclear Medicine*, 53(2), pp.171–81.

Soret, M., Bacharach, S.L. & Buvat, I., 2007. Partial-volume effect in PET tumor imaging. *Journal of nuclear medicine : official publication, Society of Nuclear Medicine*, 48(6), pp.932–45.

Spence, A.M. et al., 1998. Glucose metabolism in human malignant gliomas measured quantitatively with PET, 1-[C-11]glucose and FDG: analysis of the FDG lumped constant. *Journal of nuclear medicine : official publication, Society of Nuclear Medicine*, 39(3), pp.440–8.

Sundaram, S. & Freedman, N., 2004. Simplified kinetic analysis of tumor 18F-FDG uptake: a dynamic approach. *Journal of Nuclear Medicine*, 45(8), pp.1328–1333.

Tahari, A.K. et al., 2013. Absolute myocardial flow quantification with (82)Rb PET/CT: comparison of different software packages and methods. *European journal of nuclear medicine and molecular imaging*.

Tahari, A.K. et al., 2014. Initial human experience with Rubidium-82 renal PET/CT imaging. *Journal of medical imaging and radiation oncology*, 58(1), pp.25–31.

Takesh, M., 2012. The Potential Benefit by Application of Kinetic Analysis of PET in the Clinical Oncology. *ISRN oncology*, 2012, p.349351.

Tantawy, M.N. & Peterson, T.E., 2010. Simplified [18F]FDG image-derived input function using the left ventricle, liver, and one venous blood sample. *Molecular imaging : official journal of the Society for Molecular Imaging*, 9(2), pp.76–86.

Tong, S., Alessio, A.M. & Kinahan, P.E., 2010. Image reconstruction for PET/CT scanners: past achievements and future challenges. *Imaging in medicine*, 2(5), pp.529–545.

Tsujikawa, T. et al., 2013. In vitro and in vivo evaluation of (11)C-SD5024, a novel PET radioligand for human brain imaging of cannabinoid CB1 receptors. *NeuroImage*, pp.1–9.

Turkheimer, F.E. et al., 2007. Reference and target region modeling of [11C]-(R)-PK11195 brain studies. *Journal of nuclear medicine : official publication, Society of Nuclear Medicine*, 48(1), pp.158–67.

Valenta, I. & Schindler, T.H., 2012. (82)Rb PET/CT: entering a new area of myocardial perfusion imaging? *European journal of nuclear medicine and molecular imaging*, 39(8), pp.1231–2.

Vasquez, A.F., Johnson, N.P. & Gould, K.L., 2013. Variation in Quantitative Myocardial Perfusion Due to Arterial Input Selection. *JACC. Cardiovascular imaging*, xx(x).

Van der Weerdt, A.P. et al., 2001. Image-derived input functions for determination of MRGlu in cardiac (18)F-FDG PET scans. *Journal of nuclear medicine : official publication, Society of Nuclear Medicine*, 42(11), pp.1622–9.

Weinberg, I.N. et al., 1988. Validation of PET-Acquired Input Functions for Cardiac Studies. *J Nucl Med*, 29(2), pp.241–247.

Wong, K.-P. et al., 2002. Segmentation of dynamic PET images using cluster analysis. *IEEE Transactions on Nuclear Science*, 49(1), pp.200–207.

Wu, H.M. et al., 1995. Factor analysis for extraction of blood time-activity curves in dynamic FDG-PET studies. *Journal of nuclear medicine : official publication, Society of Nuclear Medicine*, 36(9), pp.1714–22.

Xiong, G. et al., 2012. Noninvasive image derived heart input function for CMRglc measurements in small animal slow infusion FDG PET studies. *Physics in medicine and biology*, 57(23), pp.8041–8059.

Yoshida, K., Mullani, N. & Gould, K.L., 1996. Coronary flow and flow reserve by PET simplified for clinical applications using rubidium-82 or nitrogen-13-ammonia. *Journal of nuclear medicine : official publication, Society of Nuclear Medicine*, 37(10), pp.1701–12.

Zaidi, H. et al., 2002. Fuzzy clustering-based segmented attenuation correction in whole-body PET imaging. *Physics in Medicine and Biology*, 47(7), p.1143.

Zaidi, H., 2005. *Quantitative Analysis in Nuclear Medicine Imaging* H. Zaidi, ed., New York: Springer.

Zanotti-Fregonara, P. et al., 2009. Comparison of 3 methods of automated internal carotid segmentation in human brain PET studies: application to the estimation of arterial input function. *Journal of nuclear medicine : official publication, Society of Nuclear Medicine*, 50(3), pp.461–7.

Zanotti-Fregonara, P. et al., 2011. Image-derived input function for brain PET studies: many challenges and few opportunities. *Journal of cerebral blood flow and metabolism : official journal of the International Society of Cerebral Blood Flow and Metabolism*, 31(10), pp.1986–98.

Zanotti-Fregonara, P. et al., 2012. Population-based input function and image-derived input function for [(11)C](R)-rolipram PET imaging: Methodology, validation and application to the study of major depressive disorder. *NeuroImage*.

Zheng, X. et al., 2011. A hybrid clustering method for ROI delineation in small-animal dynamic PET images: application to the automatic estimation of FDG input functions. *IEEE transactions on information technology in biomedicine : a publication of the IEEE Engineering in Medicine and Biology Society*, 15(2), pp.195–205.